

Satellite Survival in Highly Resolved Milky Way Class Halos

Sam Geen^{1,2}, Adrienne Slyz¹, Julien Devriendt^{1,2}

¹*University of Oxford, Astrophysics, Keble Road, Oxford OX1 3RH, UK*

²*CRAL, Université de Lyon I, CNRS UMR 5574, ENS-Lyon, 9 avenue Charles André, 69561 Saint-Genis-Laval, France*

7 February 2019

ABSTRACT

Surprisingly little is known about the origin and evolution of the Milky Way’s satellite galaxy companions. UV photoionisation, supernova feedback and interactions with the larger host halo are all thought to play a role in shaping the population of satellites that we observe today, but there is still no consensus as to which of these effects, if any, dominates. In this paper, we revisit the issue by re-simulating a Milky Way class dark matter (DM) halo with unprecedented resolution. Our set of cosmological hydrodynamic Adaptive Mesh Refinement (AMR) simulations, called the Nut suite, allows us to investigate the effect of supernova feedback and UV photoionisation at high redshift with sub-parsec resolution. We subsequently follow the effect of interactions with the Milky Way-like halo using a lower spatial resolution (50pc) version of the simulation down to $z = 0$. This latter produces a population of simulated satellites that we compare to the observed satellites of the Milky Way and M31. We find that supernova feedback reduces star formation in the least massive satellites but enhances it in the more massive ones. Photoionisation appears to play a very minor role in suppressing star and galaxy formation in all progenitors of satellite halos. By far the largest effect on the satellite population is found to be the mass of the host and whether gas cooling is included in the simulation or not. Indeed, inclusion of gas cooling dramatically reduces the number of satellites captured at high redshift which survive down to $z = 0$.

1 INTRODUCTION

In the standard cold dark matter paradigm of galaxy formation, galaxies grow inside dark matter halos that merge hierarchically. In other words, smaller halos are captured by larger halos and the galaxies they contain become satellite galaxies of the host galaxy until dynamical friction finally forces them to coalesce. Early attempts to reproduce the observed Milky Way satellite population using dark-matter-only simulations overproduced the number of low mass satellites by several orders of magnitude when attributing to each simulated dark matter satellite a galaxy using a constant mass-to-light ratio (Moore et al. 1999). Current state-of-the-art dark matter simulations, such as the Aquarius (Springel et al. 2008) and the Via Lactea II (Diemand et al. 2008) still reach the same conclusion.

Whilst the existing sample of Milky Way satellite galaxies is almost certainly incomplete (Koposov et al. 2008; Tollerud et al. 2008) and new satellite galaxies are continually being discovered (e.g. Belokurov et al. (2010)), it appears extremely unlikely that new observations will uncover galaxies populating every dark matter substructure predicted to exist around the Milky Way. As a result, various authors have attempted to explain this discrepancy by invoking physical mechanisms that reduce or prevent star

formation in the majority of the smaller halos, making these dark matter substructures fainter or completely dark in the process. In particular, photoionisation and feedback from supernovae have been proposed as the most likely mechanisms to prevent gas from condensing to form stars, although other mechanisms, such as cosmic rays, have also been suggested (Wadepuhl & Springel 2010).

The UV ionising background has been argued to be effective at halting or preventing star formation in low-mass halos in studies using analytic arguments, observations, N-body simulations and semi-analytic models (Efstathiou, G. 1992; Bullock et al. 2000; Benson et al. 2002; Somerville 2002; Kravtsov et al. 2004; Moore et al. 2006; Simon & Geha 2007; Strigari et al. 2007; Madau et al. 2008; Macciò et al. 2010; Muñoz et al. 2009; Busha et al. 2010). Following the pioneering work of Quinn et al. (1996); Gnedin (2000), hydrodynamic simulations of Milky Way-like galaxies have recently been employed to study the problem (Hoeft et al. 2006; Libeskind et al. 2010; Nickerson et al. 2011; Okamoto et al. 2008; Okamoto & Frenk 2009; Parry et al. 2012; Sawala et al. 2012; Scannapieco et al. 2011; Wadepuhl & Springel 2010). Many of these authors have found a best fit to the observed luminosity function by adopting instantaneous reionisation at $z \sim 11$, in agreement with the latest WMAP estimate ($z_{reion} = 10.5 \pm 1.2$

(Larson et al. 2010)). However, Hoesft et al. (2006); Wadepuhl & Springel (2010); Guo et al. (2010) also find reionisation to have limited effectiveness in completely suppressing star formation in low-mass halos that have already begun forming stars. Hoesft et al. (2006) determine that there is a characteristic mass of $6.5 \times 10^9 h^{-1} M_{\odot}$ below which halos become unable to retain baryons down to $z = 0$, and hence cannot form stars. Okamoto et al. (2008) find a similar result, which they translate into a minimum circular velocity v_{max} of 25km/s below which halos are dark. Okamoto & Frenk (2009) further refine this finding, stating that the cut-off should be lowered to $v_{max} = 12\text{km/s}$ at reionisation ($z = 9$ in their case). To further obscure the picture, the extent of the epoch of reionisation itself is poorly constrained, with only a lower limit of $z \gtrsim 6$ on its completion provided by observations (e.g. Cen et al. (2009); Mesinger & Furlanetto (2009)).

Another process is proposed in Dekel & Silk (1986). They argued that the suppression of star formation by supernova feedback in dwarf galaxies embedded in dark matter halos could explain the observed scaling relations in luminosity, metallicity and radius (Dekel & Woo 2003). Benson et al. (2003) suggested that supernovae could help explain the unexpectedly low dwarf galaxy luminosity function. By removing the gas from galaxies via the injection of thermal and kinetic energy into the interstellar medium, supernovae would reduce the number of stars formed inside dwarf halos. Authors such as Low & Ferrara (1999); Mashchenko et al. (2008); Ricotti et al. (2008); Ceverino & Klypin (2009) manage to generate massive supernova-driven galactic winds, but Tassis et al. (2008) claim that including supernova feedback does not affect the properties of their simulated galaxies, attributing the scaling relations found in dwarf galaxies to low star formation efficiencies in weak potentials instead. These contradictions find their origin in the different numerical recipes and numerical resolutions adopted, along with the variety of galaxy masses and merger histories used. As a consequence, it is still unclear as to precisely what effect supernovae have on the ISM gas, and hence on the star formation in low-mass galaxies. Indeed, supernovae are potentially able to drive either positive or negative feedback cycles. Outflows from supernovae can remove gas from the galaxy, preventing it from forming stars. However, they also release metals into the surrounding ISM; metal line cooling increases the efficiency of gas cooling and hence promotes the collapse of gas clouds into star-forming regions (Powell et al. 2011). Moreover, blast wave compression has been observed to trigger star-forming regions (Assousa & Herbst 1980).

It has also been recently (re-)suggested that our model of dark matter is incorrect. Boylan-Kolchin et al. (2011); Lovell et al. (2012); Di Cintio et al. (2011) examine the relationship between the maximum circular velocity of the dwarf spheroidal satellites and the radius at which this velocity is found, and determine that the velocities found are higher than those found in either Λ CDM pure dark matter simulations or simulations with baryon physics using smoothed particle hydrodynamics (SPH). In fact, Di Cintio et al. (2011) determine that gas cooling makes the problem worse, since the central density of the halo increases and the radius at which the maximum circular velocity is found decreases. Lovell et al. (2012) suggests that warm dark matter (WDM)

resolves the problem, but they do not run simulations with both WDM and baryon physics.

Bearing these caveats in mind, the present paper aims to constrain satellite galaxy formation and evolution, and more specifically the role played by supernova feedback and reionisation in the process. To this end, we use the `nut` (NUT) suite of high resolution hydrodynamic cosmological simulations of a Milky Way-like galaxy (Powell et al. 2011; Kimm et al. 2011). At scales of 1-10pc, these resolve large molecular clouds, and hence model the interstellar gas and stellar feedback in greater detail, which potentially affects star formation histories (Slyz et al. 2005). This approach differs from previous work investigating the Milky Way satellites using hydrodynamic simulations as these generally capture the ISM at lower resolution, and attempt to compensate for this by introducing analytic expressions to account for the multiphase ISM and outflows (Scannapieco et al. 2005, 2006; Murante et al. 2010). As it is currently too costly to simulate a Milky Way-sized halo and its substructures with parsec resolution and hydrodynamics throughout the lifetime of the Universe, most of our analysis is restricted to high redshift ($z > 6$). However, observational studies conclude that a vast majority of satellite galaxies contain stars which formed prior to $z \sim 2$ and in many cases prior to even $z \sim 5$ (see recent review by Tolstoy et al. (2009) and also Kirby et al. (2011)). Therefore, a high redshift study of these objects should be able to shed light on the problem, provided one is able to accurately predict their spatial distribution at $z = 0$.

This latter requirement is in itself a major challenge as it presumably requires hydrodynamics simulations which include (at least) radiative cooling. Indeed, since gas cooling can significantly increase the central density of dark matter halos (e.g. Blumenthal et al. (1984)), one expects physical processes like dynamical friction and tidal disruption of the satellites to be altered. The extent of these differences needs to be quantified because most of the studies mentioned earlier in this introduction rely on pure dark matter simulations to underpin analytic arguments or graft semi-analytic models of galaxy formation. Several groups have looked at differences between simulations of galactic halos containing baryons and their pure dark matter N-body counterparts. For instance Peirani (2010) found that identical simulations of a local group-like volume with and without baryons matched well, but did not comment on satellites within halos. In their constrained simulations of the Local Group, Libeskind et al. (2010) find more satellite halos when baryons are included than in the identical pure dark matter run. Their radial distribution is also significantly more concentrated. By contrast, although they also follow a more concentrated radial distribution, satellites in the baryonic simulations of Romano-Díaz et al. (2010, 2009) survive for shorter times than their pure dark matter counterparts, which yields an overall lower number of satellites within R_{vir} when baryons are included. Schewtschenko & Macciò (2011) finds a similar result to Libeskind et al. (2010) in terms of number of halos but suggests that these results are not incompatible with those of Romano-Díaz et al. (2010). We re-examine this issue using Eulerian AMR grid hydrodynamics instead of Lagrangian smoothed particle hydrodynamics (SPH), and improving on both mass and force resolution for the dark matter.

This paper is split into three main parts. In section 2, we describe the simulations, our algorithms for comparing them and for tracking halos at high redshift down to $z = 0$. Section 3 looks at the effect of feedback mechanisms on satellite galaxy formation at high redshift and ultra-high resolution. The third part, section 4, is devoted to the present epoch, and how our results at high redshift affect the satellite population we see today.

2 METHODS

In this section we discuss the methods employed to carry out the simulations used in this paper and the subsequent analysis techniques.

2.1 Numerical simulations

We analyse five simulations in the NUT suite of simulations (NUT is the Ancient Egyptian goddess of the sky) (Powell et al. 2011; Kimm et al. 2011). NUT is a set of cosmological hydrodynamic resimulations of a Milky Way-like halo at $z = 0$ (throughout this paper, this halo will be referred to as the “Milky Way”). To run these simulations, we use the Adaptive Mesh Refinement (AMR) code RAMSES (Teyssier 2002). Each simulation starts from identical initial conditions, which are generated with MPGRAFIC (Bertschinger 2001; Prunet et al. 2008) using cosmological parameters consistent with the WMAP 5 year measurements (Dunkley et al. 2009). The simulation volume is a periodic, cubic box of length $9h^{-1}\text{Mpc}$ with a minimum resolution of 128^3 dark matter particles and the same number of grid cells. Within this volume we carve out a spherical region of radius $1.44h^{-1}\text{Mpc}$, centred on a halo that reaches a virial mass $M_{\text{vir}} = 5 \times 10^{11}M_{\odot}$ at $z=0$. We place three nested grids in this spherical region with effective resolutions of 256^3 , 512^3 and 1024^3 dark matter particles and grid cells. The minimum dark matter particle mass inside this region is equal to $5.6 \times 10^4 M_{\odot}$ (with the exception of the Dark Matter run, which we describe later in this section). We then allow the grid inside the refinement region to adaptively refine up to a given maximum level for each simulation. Our refinement strategy is quasi-Lagrangian: a grid cell is refined when the number of dark matter particles in the cell exceeds 8, or the baryonic mass of the cell reaches $8 m_{\text{SPH}}$, where $m_{\text{SPH}} = 9.4 \times 10^3 M_{\odot}$. The simulation parameters used are summarised in table 1, and in the text below.

The three main simulations that we consider in this paper contain dark matter, gas cooling and a uniform UV background switched on at $z = 8.5$ to model reionization (Haardt & Madau 1996). Gas cooling is modelled as radiative energy loss from atomic processes including emission line cooling (below 10^4K), with a primordial metallicity of $0.001 Z_{\odot}$. Star formation in the simulation proceeds according to a Schmidt law on a local dynamical timescale (Cen & Ostriker 1992) with an efficiency of 1%. The density threshold for star formation is set in each simulation to be comparable to the corresponding Jeans density of a cell on the highest level of refinement with a temperature of 100K .

We first run a simulation that we call the “Reference run”. The Reference run is allowed to refine

adaptively to up to 8 times inside the fixed refinement region, such that the densest regions are allowed to reach a maximum physical resolution of 50pc at all times, between a few times and an order of magnitude higher than other cosmological hydrodynamics simulations of Milky Way satellites (Libeskind et al. 2010; Nickerson et al. 2011; Okamoto & Frenk 2009; Parry et al. 2012; Ricotti & Gnedin 2005; Romano-Díaz et al. 2010, 2009; Sawala et al. 2012; Scannapieco et al. 2011; Schewtschenko & Macciò 2011; Wadepuhl & Springel 2010). The minimum star particle mass in this simulation is $3.5 \times 10^4 M_{\odot}$. We run this simulation to $z = 0$. Note that the main purpose of this run is to act as a lower spatial resolution “twin” of the two “high resolution” simulations in this study, allowing us to determine which of the galaxies formed at high redshift are progenitors of Milky Way satellite galaxies today. For this reason the DM mass resolution is kept identical in all runs. The threshold for star formation in the Reference run is 10 atoms/cm^3 .

We then run two high resolution simulations which are allowed to refine adaptively by up to 15 times so that its physical spatial resolution in the densest regions can reach a maximum of 0.5pc at all times. The first of these high resolution simulations we call the “Cooling run”. As with the Reference run, the Cooling run contains dark matter, gas cooling and a uniform UV background switched on at $z = 8.5$, but now the threshold density for star formation is 10^5 atoms/cm^3 . As a result, the minimum star particle mass formed in the Cooling run is $167M_{\odot}$. The second of the high resolution simulations is called the “Feedback” run. The Feedback run is identical to the Cooling run, except that it also includes supernova feedback. Following Dubois & Teyssier (2008), supernovae are implemented as Sedov blast waves with a radius of 2 grid cells (1pc) around a star particle 10 Myr after it formed. Note that while we do not resolve individual stars, at this mass resolution and assuming a Salpeter initial mass function (Salpeter 1955), we get one supernova per star particle. We assume supernova events entrain 50% of the initial mass of the star particle ($\eta_{\text{W}} = 1$ in the notation of Dubois & Teyssier (2008)) in a wind and have a metal yield of 0.1. The energy released is given by $\eta_{\text{SN}} \frac{m_{\star}}{m_{\text{SN}}} e_{\text{SN}}$, where m_{\star} is the mass of the star particle, m_{SN} and e_{SN} are typical values for a massive star going supernova and η_{SN} is the fraction of the total mass formed that is turned into supernova ejecta. For this simulation, we use $\eta_{\text{SN}} = 0.106$, $m_{\text{SN}} = 10M_{\odot}$ and $e_{\text{SN}} = 10^{51}\text{ergs}$ (Powell et al. 2011; Kimm et al. 2011). This translates into a minimum star particle final mass of $76M_{\odot}$ for the Feedback run.

Finally, we perform a further two simulations. These are called the Dark Matter run and the Adiabatic run. Both have the same initial conditions and refinement criteria as the Reference run. The Dark Matter run is a pure N-body dark matter simulation, in which the mass in baryons is replaced by mass in dark matter, giving it a minimum dark matter particle mass of $6.7 \times 10^4 M_{\odot}$ rather than $5.6 \times 10^4 M_{\odot}$ which is the value common to all the other runs. The Adiabatic run is identical to the Reference run, except that the gas is not permitted to radiate away its energy. As a result, no star formation takes place in the Adiabatic run, though we still include the UV background for sake of comparison. These two simulations are used to determine the effect of

Simulation	z_{min}	m_{DM}	R_{max} (level)	Gas Cooling	m_*	SNe	UV
Reference Run	0	$5.6 \times 10^4 M_\odot$	50pc (18)	✓	$3.5 \times 10^4 M_\odot$		✓
Cooling Run	6.7	$5.6 \times 10^4 M_\odot$	0.5pc (25)	✓	$167 M_\odot$		✓
Feedback Run	6.7	$5.6 \times 10^4 M_\odot$	0.5pc (25)	✓	$76 M_\odot$	✓	✓
Dark Matter Run	0	$6.7 \times 10^4 M_\odot$	50pc (18)		-		
Adiabatic Run	0	$5.6 \times 10^4 M_\odot$	50pc (18)		-		✓

Table 1. Table of properties of numerical simulations included in this paper. The columns are, from left to right, the simulation name, the lowest redshift reached by the simulation, the minimum dark matter particle mass, the maximum spatial resolution of the AMR grid (with the associated level of refinement in brackets), whether the simulation includes gas cooling, the minimum star particle mass, whether the simulation includes supernova feedback, and whether the simulation includes a UV background. The bottom two simulations are considered only in section For a complete description of the simulations, see section 2.1.

including more physics on satellite galaxy evolution from $z \sim 6$ (the redshift where the high resolution simulations stop) to $z = 0$. We discuss the results of this study in section 4.3 and compare the Dark Matter run to other pure N-body dark matter simulations of Milky Way satellites in section 4.2.

2.2 Halo identification

We use HaloMaker to identify dark matter halos and galaxies in each simulation output using the Most Massive Subhalo Method (MSM) (Tweed et al. 2009). We identify independent halos as dark matter overdensities not contained within another halo, and subhalos as halos that are identified as substructures of other halos. Similarly, we identify galaxies as overdensities in the star particles. For this procedure, we reject any identified halo that contains less than 40 particles, and any galaxy that contains less than 10 particles. The minimum total mass of a given dark matter (sub)halo is thus $2.2 \times 10^6 M_\odot$ and the minimum stellar mass for a galaxy is $3.5 \times 10^5 M_\odot$ in the Reference run, $1700 M_\odot$ in the Cooling run and $760 M_\odot$ in the Feedback run.

We perform this process in every simulation for both the dark matter and the stars whenever possible. We thus identify every dark matter halo and every galaxy above the mass limits given in the last paragraph. We visually inspect the results of the halo identification and tune the halofinder parameters such that we minimise spurious halo detection or halos that are visually identifiable but not detected by the halo finder.

We then identify the host halo of galaxies to determine which halos are luminous and which are dark. This sorting proceeds in two steps: (i) for each galaxy, we make a list of halos that enclose it within their virial radius (ii) we select the halo that lies closest to the galaxy centre. This final step is needed when the galaxy’s host is a subhalo of a larger halo, and the galaxy lies within the virial radius of both the subhalo and its host. This allows us to match halos between runs and to compare the properties of the embedded galaxies in each simulation on an individual halo basis.

2.3 Halo twinning

In order to compare the simulations, we associate each halo in the Reference run with a counterpart (called ‘twin’) in the Cooling and Feedback runs. As well as allowing us to compare halos between different runs at common redshifts, this procedure also permits us to track the halos in the Cooling

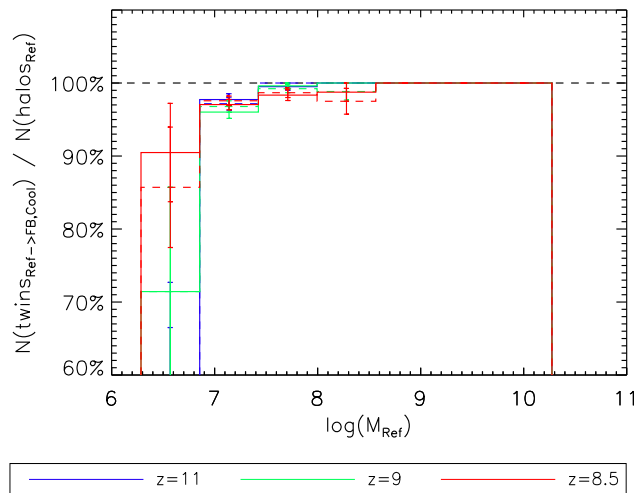


Figure 2. Histograms of percentage of halos in each mass bin in the Reference run with twins in the Cooling and Feedback run against virial mass in the Reference run in M_\odot . The error bars show the sampling error on the number of un-twinning halos in each bin. The colours correspond to the values at different redshifts (see legend). Twins in the Feedback Run are shown with a solid line, and twins in the Cooling Run are shown with a dashed line. For halos of mass greater than $10^7 M_\odot$, we find a success rate above 95% in the twinning procedure. For halos below $10^7 M_\odot$ (less than 200 DM particles) and at higher redshifts, this rate drops quite rapidly because of the lower spatial (force) resolution in the Reference run which reduces the overall number of collapsed objects.

and Feedback runs down to $z = 0$ via the merger trees of their counterparts in the Reference run (see section 2.4).

We adopt a twinning strategy similar to Libeskind et al. (2010); Peirani (2010); Romano-Díaz et al. (2010, 2009); Schewtschenko & Macciò (2011). A list of particles and associated halo ID numbers is found for each halo in each simulation for each output in the Reference run. Due to the differences in the timestepping in each simulation there is typically 0.5-1Myr difference between a given Reference run output and a given output in the Cooling and Feedback runs. The list of halos in the Reference run is sorted in descending order of halo mass. Particles in the Reference run list are removed if they are not in halos in the Cooling or Feedback run. If a certain halo in the Reference run has fewer than 50% of its particles in halos in the Cooling or Feedback run, it is considered to have no identifiable counterpart in the other simulations and is hence ignored.

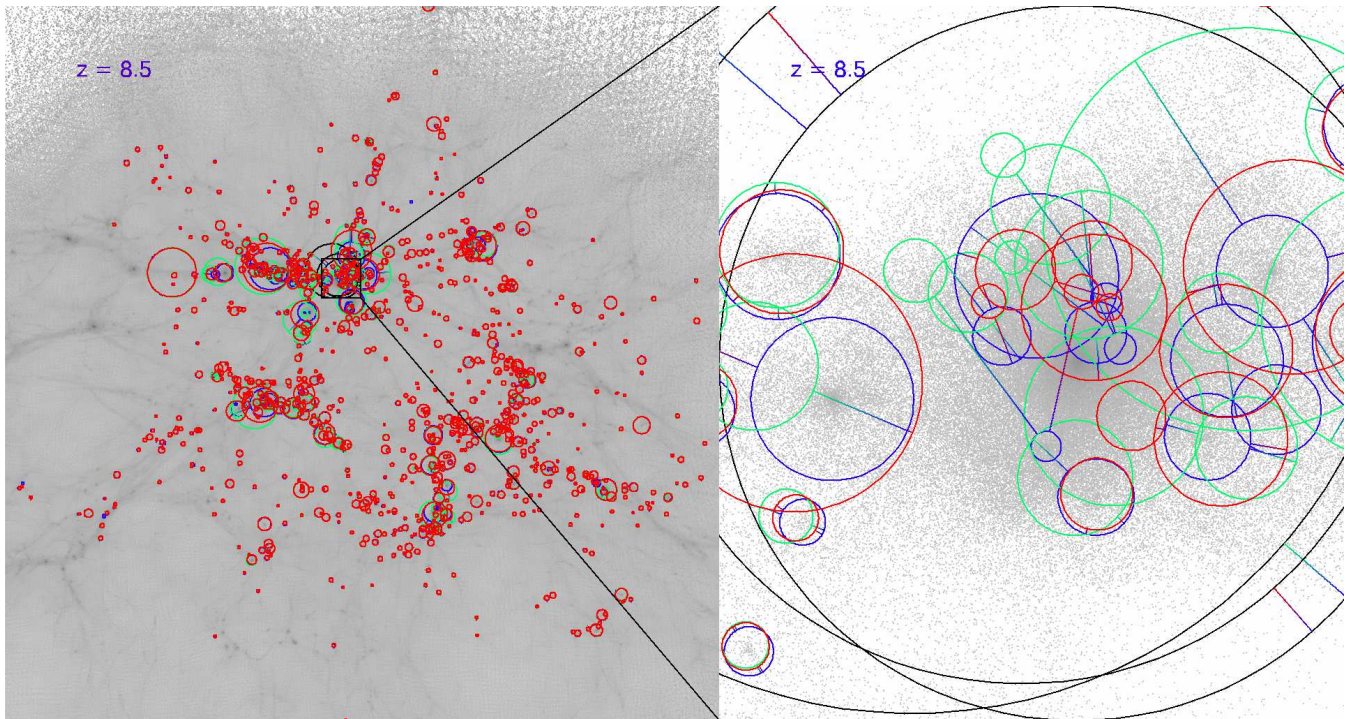


Figure 1. Visualisation of the halo twinning results at $z = 8.5$. The left panel shows the cubic volume (300kpc on a side) containing all the Milky Way satellite progenitor dark matter halos identified by $z = 0$. The right panel shows a zoom on the Milky Way progenitor halo outlined by the black square in the left image. The grey scale background represents the dark matter projected density distribution in the Reference run. Overlaid circles indicate the virial radii of halos identified as being Milky Way progenitors in the Reference run (blue) and their twins in the Cooling (green) and Feedback (red) runs, with colours overplotted in that order (hence halos with very similar positions and radii in all three runs appear as red circles). In the right-hand image we connect the halo in the Reference run with its twin in the other runs via straight lines. The Milky Way progenitor halo in each run is shown in black. Most of the twins are remarkably well matched in size and position, although unsurprisingly, the subhalos of the Milky Way progenitor show more pronounced discrepancies between runs, especially in the central region of the halo.

For each halo in the Reference run we calculate the fraction of its particles that belong to a halo in the Cooling and Feedback runs. We then select the single halo from each of the Cooling and Feedback runs that has the largest fraction of its particles in the Reference run halo and has not already been assigned to another Reference run halo. This provides a 1:1 mapping between the halos of any two simulations.

In order to visually confirm that the twinning procedure works, we plot a map of the Reference run’s projected dark matter density field in Fig. 1. On the same figure, we overplot halos in the Reference, Cooling and Feedback runs as circles with radii proportional to their virial radius. We also link the halos in the Reference run to their twins in the Cooling and Feedback runs with straight lines connecting the corresponding circles. The figure clearly shows that in general, the twinning procedure yields excellent results for most halos (the vast majority of circles in the left panel of Fig 1 are red). For the region encompassed by the Milky Way progenitor (the right-hand zoomed-in panel), twinning results are still quite good, except in the very centre where positions and sizes of sub-halos diverge as the non-linear nature of the system (shell-crossing) and the slight differences in output times between the runs begin to plague the comparison.

A quantitative analysis of the twinning procedure reveals that the Reference run has 96.4% of its halos twinned

with the halos in either the Feedback or Cooling run at $z=6.7$ (the final redshift for which all runs have data). If we relax the 1:1 mapping criterion and simply consider halos above the threshold where 50% of their particles in the Reference run also are found in halos in the other runs, 98.6% of halos have twins. In Fig. 2, we plot the success rate for twinning halos as a function of mass and redshift for the Feedback (solid lines) and Cooling runs (dashed lines). We find that for halos over $10^9 M_\odot$ there is a 100% success rate for the twinning procedure regardless of redshift. This success rate remains over 90% above $10^7 M_\odot$ (i.e. for halos containing $\gtrsim 200$ DM particles). For halos below this mass, the lower resolution of the Reference run causes the success rate of the twinning procedure to drop to between 70-90%. Note that only the *spatial* (or force) resolution in the Reference run is lower than in the Cooling or Feedback runs; the dark matter mass resolution is identical.

2.4 Tracking high redshift galaxies down to $z = 0$

The ultimate goal of this project is to compare our simulated galaxies to observed Milky Way satellites. In order to achieve this, we need to evolve our simulated galaxies in the Cooling and Feedback run to $z = 0$. Since it is computationally unfeasible at their nominal resolution, we instead track their evolution via their twin halos merger trees in the Ref-

erence run. This determines which galaxies at high redshift are the progenitors of Milky Way satellites today and allows us to quantify how advanced satellite galaxy formation is by the end the epoch of reionisation.

The fundamental assumption we make is that a halo which already contains stars at high redshift will still contain a galaxy at $z = 0$. This assumption is extremely plausible for two reasons. Firstly, even the lowest-mass halos are observed to be dark-matter dominated (Strigari et al. 2008), and thus we do not expect to find galaxies without dark matter halos. Secondly, galaxies are all predicted to be embedded within the inner part of the halo in which they form, so that the galaxy will be the last part of the halo to be destroyed, with tidal stripping affecting the outer regions of the halo first (e.g. Peñarrubia et al. (2010)). We further comment on the validity of this assumption in section 4.4 where we identify galaxies in the Reference run at $z=0$ and locate their dark matter host halos. Finally, we also assume with this extrapolation technique that the dynamical friction and tidal stripping experienced by the satellite halos in the Reference Run are similar to the Cooling and Feedback runs, i.e. that increased resolution and supernova feedback do not dramatically alter their efficiency. We discuss the validity of this assumption in more detail in section 4.3.

We build the merger tree for the Reference run using the technique described in Tweed et al. (2009). As in section 2.3, we use the particle IDs to track dark matter particles between snapshots. For every halo in a given snapshot we build a list of halos in the following snapshot that contain particles from this halo. We then select the halo that contains the most particles from this halo as its ‘child’ halo, adopting a ‘one child’ policy. By doing this, we create a halo merger tree where if halo C in output 3 is a child of halo B in output 2 and halo B is a child of halo A in output 1, then halo C is also a child of halo A. One side-effect of this method is that if a subhalo loses more than 50% of its particles between two outputs, that subhalo is assumed to have been completely stripped by its host. To limit this occurrence, we use a large number of snapshots to build our merger tree (~ 100), so that our effective time resolution is roughly 150Myr. Note that this method compares favourably to a second, more straightforward method we attempted, in which halos are directly matched between a single high-redshift output and the output at $z = 0$. In this alternative method, we chose as the ‘child’ the halo at $z = 0$ that was given the largest proportion of its particles by the high redshift halo. However the inevitable high mass loss rates between high and low z outputs led to a few pathological cases whereby the ‘same’ halo at two different high redshift outputs was attributed different children at $z = 0$. For this reason, we use the merger tree method for all further analysis.

2.5 Resolution effects on galaxy formation

In order to assess how reliable the Reference run is to locate satellite galaxies at $z = 0$, we first compare it to the higher resolution Cooling and Feedback runs in the redshift range where all the runs overlap. In section 2.3, we showed that we are able to very successfully match halos more massive than $10^7 M_\odot$ between simulations. We now consider the effect that resolution has on star formation.

As previously mentioned in section 2.1, the Reference

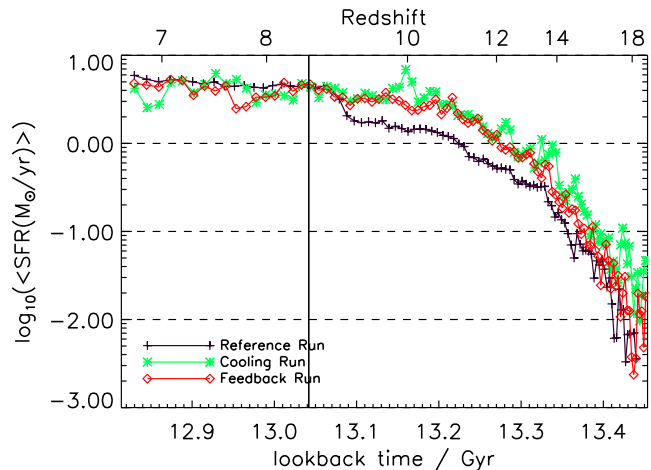


Figure 3. Star formation rate averaged over all halos in each simulation. The Reference run is shown in black, the Cooling run in green and the Feedback run in red. The vertical black line shows the time ($z = 8.5$) at which the universe is reionised in the simulation. Star formation in the Reference run is slightly delayed compared to the other runs, but catches up before reionisation. The jump in star formation rate at $z = 9$ is due to the triggering of a new level of refinement on the grid (from 14 to 15 levels) at this redshift, which allows the gas to collapse further and triggers star formation in all potentially star-forming halos.

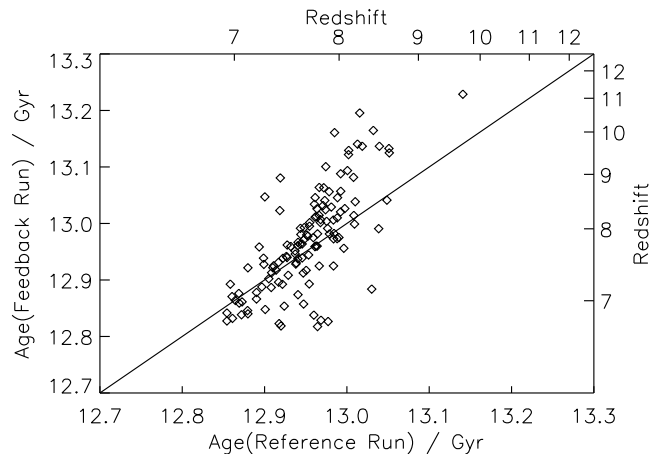


Figure 4. Comparison of the mass-weighted stellar age for halos in the Reference run and their twins in the Feedback run. Halos that lie on the diagonal black line have the same mass-weighted stellar ages in both runs. Due to its lower resolution, as explained in section 2.5, the Reference run generally forms stars later than the Feedback run. However, the difference in star formation parameters between the runs allows a modest fraction of halos to form stars before, especially at lower redshifts. Similar results are found when comparing the Reference run to the Cooling run.

run has the same dark matter mass resolution as the Cooling and Feedback runs. However, the spatial resolution, which determines the accuracy of both the gravitational force and the properties of the gas is lower; 50pc in the Reference run instead of 0.5pc in the Cooling and Feedback runs. The density threshold for star formation is therefore lowered from 10^5 atoms/cm^3 at high resolution down to 10 atoms/cm^3 at low resolution, whilst the efficiency of star formation is preserved.

In figure 3, we compare the global star formation rate of halos in each of the runs. We find that before a lookback time of 13.1 Gyr ($z = 9$), the Reference run's star formation rate is roughly half that of the Cooling and Feedback runs. However, after 13.1 Gyr, all star formation rates agree within 30% percent. This difference of behaviour before and after 13.1 Gyr has nothing to do with reionisation, which occurs later on. Indeed this effect is purely numerical, and induced by the refinement criteria we choose to enforce. RAMSES refines the AMR grid using an octree, meaning that spatial resolution is a power-of-two fraction of the total box length (Teyssier 2002). Since we specify a maximum spatial resolution for the grid in physical parsecs, we trigger a power-of-two increase in resolution each time the cosmological scale factor has increased enough that an extra level is necessary to achieve such a resolution. In the Reference run, such a jump in refinement level from 14 to 15 happens around $z = 9$. Rasera & Teyssier (2006) demonstrate that too low a maximum spatial resolution delays the collapse of low mass haloes/galaxy disks, preventing the ISM gas density in many of them from crossing the star formation threshold until a higher level of resolution is achieved. Such a delay eventually vanishes when the maximum spatial resolution becomes sufficient *at all times* as the lack of 'step' in the star formation histories of the Cooling and Feedback runs on Fig 3 clearly shows.

The good agreement between the global star formation rates of all three runs for lookback times smaller than 13.1 Gyr is expected by construction. This is because we select the density threshold for the Reference run to best match the star formation measured in the Cooling and Feedback runs. This has to obey two constraints: (i) the star formation density threshold should be smaller than the corresponding Jeans density ($\rho_J = (\pi c_s^2)/(\lambda_J^2 G) \sim 40 \text{ at/cm}^3$ (Binney & Tremaine 2008)) on the highest level of refinement and (ii) stars should not form in smooth filaments, which yields a lower bound on the density threshold that we empirically determine to be $\sim 10 \text{ at/cm}^3$ (Powell et al. 2011). Alternative Reference runs with different values of the density threshold led to the conclusion that the lowest bound (10 atoms/cm^3) matches the global star formation histories in the Cooling and Feedback runs best, as shown on Fig 3.

We now consider the agreement between star formation histories of individual galaxies. In Fig. 4, we compare the mass weighted stellar ages of galaxies simulated at low (Reference run) and high (Feedback run) resolution and twinned at $z = 6.7$. We find a pattern similar to that of the global star formation histories presented in Fig 3; namely star formation is delayed in the Reference run but converges to values similar to the Feedback run at a lookback time comprised between 13.0 and 12.9 Gyr. After this epoch there is some inevitable scatter due to the nonlinear nature of star formation, but this scatter is centred around the line of equal age in Fig. 4. The lookback time at which the ages converge is later than the jump in star formation due to resolution because the mean age is skewed by the relative paucity of stars formed before 13.1 Gyr in the Reference run (Fig. 3). A similar result is found when comparing the Cooling run to the Reference run.

It is worth pointing out that the location of star formation within a galaxy is not guaranteed to match between

simulations. Star formation in the Cooling and Feedback runs is confined to regions with densities similar to molecular cloud cores ($\rho > 10^5 \text{ atoms/cm}^3$), whereas in the Reference run star formation is allowed to occur in regions where the density is closer to that of typical diffuse clouds (10 at/cm^3). However, for analysing the bulk properties of satellite galaxies between reionisation and $z = 0$ this distinction is largely irrelevant.

3 FEEDBACK IN MILKY WAY SATELLITE PROGENITORS

3.1 Supernova Feedback

We now discuss the differences between the simulations with and without supernova feedback, in order to better understand the role of supernovae in high-redshift dwarf galaxy and Milky Way satellite formation. We use the twinning method described in section 2.3 to match halos in the Cooling and Feedback runs. We can thus determine whether the net effect of including supernovae in our sub-parsec resolution simulations enhances or suppresses star formation in halos of various masses. Fig. 5 shows images of the main progenitors of the Milky Way and each of its satellites at $z = 6.7$. We find that every satellite progenitor has supernova outflows of different sizes, evidenced by metal-enriched outflows from the galaxy. Whether galaxies at $z = 6.7$ become satellite galaxies of the Milky Way at $z = 0$ or are disrupted by interactions with the Milky Way halo is discussed in section 4.1.

Powell et al. (2011) discuss the differences in gas temperature and density when adding supernova feedback using phase diagrams of the Milky Way progenitor in the Cooling and Feedback runs. We now perform a similar study for a sample satellite galaxy progenitor. Fig. 6 shows typical phase diagrams for a star-forming halo at $z = 6.7$ (halo 'g' in Fig. 5) inside r_{vir} for each run. Following Powell et al. (2011), the phase diagram can be divided into distinct sections.

The first is the cold dense phase, containing the gas filaments. This gas, at a temperature $\sim 10^4 \text{ K}$ and densities comprised between $\sim 10^{-2}$ and 1 at/cm^3 accounts for a large fraction of the total gas in the halo, as shown by the colour coding in Fig. 6 where blue represents the largest mass fraction. Above $\sim 1 \text{ at/cm}^3$, the ISM begins and the temperature begins to drop below 10^4 K especially in the presence of metals (Feedback Run). The vertical dash-dot lines in Fig 6 shows the densities at which we allow star formation to occur (10 at/cm^3 in the Reference run and 10^5 at/cm^3 in the Cooling and Feedback runs).

The final phase in Fig. 6 is the warm/hot diffuse phase, which represents gas that has been heated to or above the virial temperature of the halo. The Cooling and Feedback runs both produce gas in this phase. In both runs, a small quantity of gas falling into the halo diffusely, outside of the cold filaments, shock-heats. Due to its lower resolution, the Reference run does not exhibit this effect. In addition to this shock heated material, the Feedback run shows extra low-density hot gas originating from supernova explosions. These heat gas and potentially remove some from the centre of the halo, reducing star formation.

We now proceed to quantify to which extent the positive

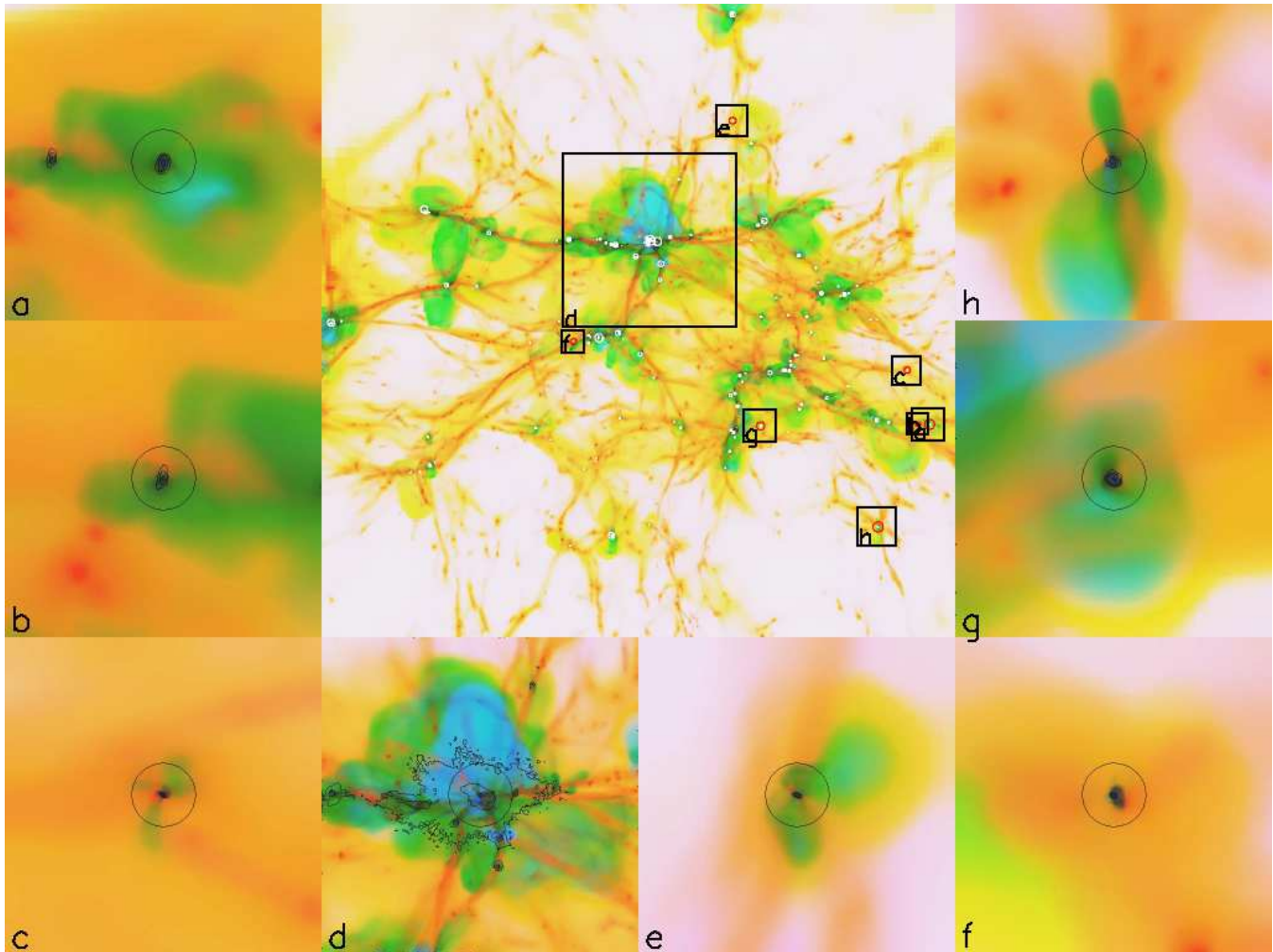


Figure 5. Progenitors of the Milky Way satellite galaxies formed before $z=6.7$ in the Feedback Run. The colour map shows projections of the density in red, the density-weighted temperature in yellow and the metallicity in green (highlighting the metal-enriched galactic outflows). The outer images are cubic projected images of satellite progenitors with a length of 10 dark matter virial radii, with the stellar column density overplotted as contours in black. The central image is a cubic projection of the full refinement region. White circles in the central image are galaxies, and red circles are halos containing galaxies that survive to become Milky Way satellites at $z = 0$ in the Feedback Run. The labels ‘a’-‘h’ indicate the position of the individual satellite images on the central image, with black boxes marking the size of the outer image on the central image. The Milky Way main progenitor is labelled ‘d’.

feedback processes (metal cooling, blastwave compression) or negative feedback processes (gas heating, outflows) dominate in halos of different masses. In Figs 7 and 8, we plot comparisons of the total gas mass, star-forming gas mass and total stellar mass in each halo in the Cooling and Feedback runs, using the halo twinning procedure described in section 2.3. Star-forming gas is defined as gas with a density above 10^5 at/cm^3 our density threshold for star formation. In each figure we overplot the median and interquartile range of the fractional differences in the mass bins $10^7 M_\odot - 10^8 M_\odot$, $10^8 M_\odot - 10^9 M_\odot$ and $10^9 M_\odot - 10^{10} M_\odot$. For the gas masses, since there exists a large scatter in the results we plot the ratio for each halo on a log scale to highlight both large and small differences. For the stellar masses, since differences are smaller, we plot the fractional difference between the runs. In other words, if we denote the ratio between stellar masses by R , we plot the quantity $(R - 1)/(0.5(R + 1))$.

Although Fig 7 shows a large scatter in ratios of gas

masses of twinned halos in the Cooling and Feedback runs, the median values lie around an equal ratio, with the $10^7 M_\odot$ to $10^8 M_\odot$ mass bin showing $\sim 5\%$ less gas and the halos in the higher mass bins having a similar or slightly higher gas content in the Feedback run. This goes in the expected direction since supernovae eject gas back into the galaxy, causing the total gas mass to increase if this ejecta is unable to escape the halo. There is also considerably more scatter in the instantaneous star-forming gas mass results, with some halos in the Feedback run containing over 100 times the mass of star-forming gas than their Cooling run twins. This effect can be attributed to the enhanced metal cooling which takes place after the first supernovae explode in the Feedback run. However, on average we find a similar pattern to the total gas mass ratios, i.e. lower mass halos in the Feedback run contain very slightly less star-forming gas than their Cooling run counterparts, and more massive halos slightly more. That said, at $z = 8.5$ the highest mass bin has a median star-

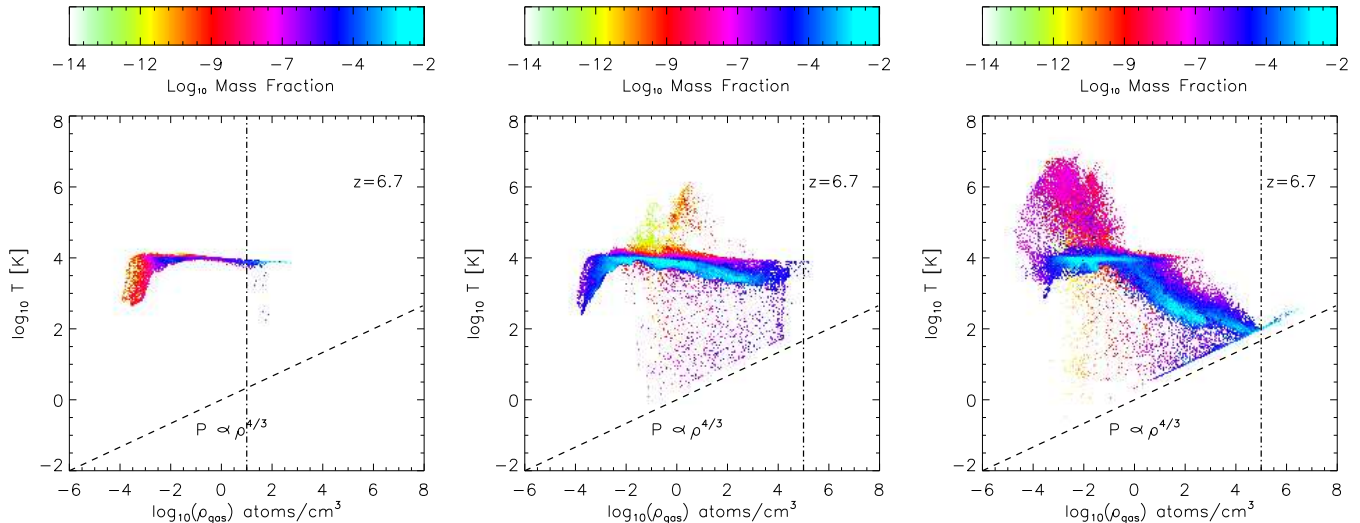


Figure 6. Phase diagrams of the gas inside r_{vir} of a single satellite progenitor at $z = 6.7$ (halo ‘g’ in Fig. 5). On the left is the Reference run, in the middle is the Cooling run and on the right is the Feedback run. The bulk of the gas in the halo is just below the T_{vir} ($\sim 10^4$ K). The Feedback run exhibits high-temperature plumes corresponding to supernova-heated gas, while the Cooling run shows a tiny fraction of shock-heated infalling material. The Reference run does not contain any gas heated above the virial temperature. There is more cold, dense gas in the Feedback run than in the Reference and Cooling runs due to more efficient cooling from the injection of metals into the gas by supernovae. The dashed line shows the polytropic equation of state $P \propto \rho^{4/3}$, which is imposed between T and ρ to avoid numerical fragmentation. The vertical dot-dash line shows the density above which star formation can occur (10 at/cm^3 in the Reference run and 10^5 at/cm^3 in the Cooling and Feedback runs).

forming gas mass that is twice as high. The large scatter in the amount of star-forming gas is expected; Stinson et al. (2007) also find that star formation in their dwarf galaxies is quite bursty, because the instantaneous mass of star-forming gas can strongly fluctuate on short timescales, driven by catastrophic non-linear events (instabilities, mergers).

Motivated by this result, in Fig. 8 we plot a time integrated quantity – the fractional difference between the stellar mass of each twinned halo that has formed stars in the Cooling and Feedback runs. Unsurprisingly, there is a maximum 20% difference between values, much smaller than that for the star-forming gas mass. For similar reasons, we also find more scatter in stellar mass ratio of low mass halos than of high mass halos: the length of time that lower-mass halos have been forming stars is generally shorter. Therefore, they are more affected by temporary fluctuations in their star formation histories. As with the gas mass comparison, we find that the positive feedback processes outweigh the negative feedback processes in the highest mass bin, leading to a net increase in the median fractional difference in stellar mass of a few percent when supernova feedback is added.

In summary, we find that the effect of feedback on the gas mass and star formation in a halo is complex, with lower mass halos being on average more affected by negative feedback processes such as outflows and gas heating, and higher mass halos by positive feedback processes such as blastwave compression and metal cooling. We also find that stellar masses in individual twin halos can differ by up to 20%; however, the median values only differ by a few percent in all mass bins, although values for low mass halos are more scattered. We therefore conclude that supernovae do not seem to have a significant effect on Milky Way satellite progenitors, at least at redshifts larger than 6.

3.2 Reionisation Feedback

At $z = 8.5$ in each simulation we include a simple instantaneous, uniform heating term that represents the UV background according to the model of Haardt & Madau (1996). There are two ways such a background affects galaxy formation/evolution in our simulations: (i) it heats the ISM, which could prevent the gas density within galaxies from crossing the star formation threshold, and (ii) it heats the IGM, which could cut off the gas accretion onto galaxies. Note that we very likely overestimate these effects in the simulation as we neglect self-shielding which is known to occur around densities $n_H \lesssim 0.1$ at/cm^3 (Susa & Umemura 2004). On the other hand, we do not account for the local UV radiation (from stars within the galaxy itself) which also photo-ionises the ISM/IGM. Nevertheless, by looking at the star formation rate in halos before and after $z = 8.5$, we should be able to estimate how efficient non-local ionisation is at halting star formation.

Fig. 9 shows that reionisation does not immediately stop star formation in halos already forming stars, in agreement with Kitayama et al. (2001); Machacek et al. (2001); Gnedin & Kravtsov (2006); Okamoto & Frenk (2009); Wadepuhl & Springel (2010). Even for the lowest mass halos ($M_{vir} < 10^8 M_\odot$), we find that star formation continues after the uniform UV background is turned on. The free-fall time of a test particle falling from r_{vir} into one of the smallest galaxies formed at $z = 8.5$ is on the order of 50 Myr. Hence, we conclude that star formation is not stopped in these halos even after ~ 5 free-fall times (the amount of time elapsed between $z = 8.5$ and $z = 6.7$). In other words, if reionisation does halt star formation by heating up the ISM or cutting off the gas accretion in halos

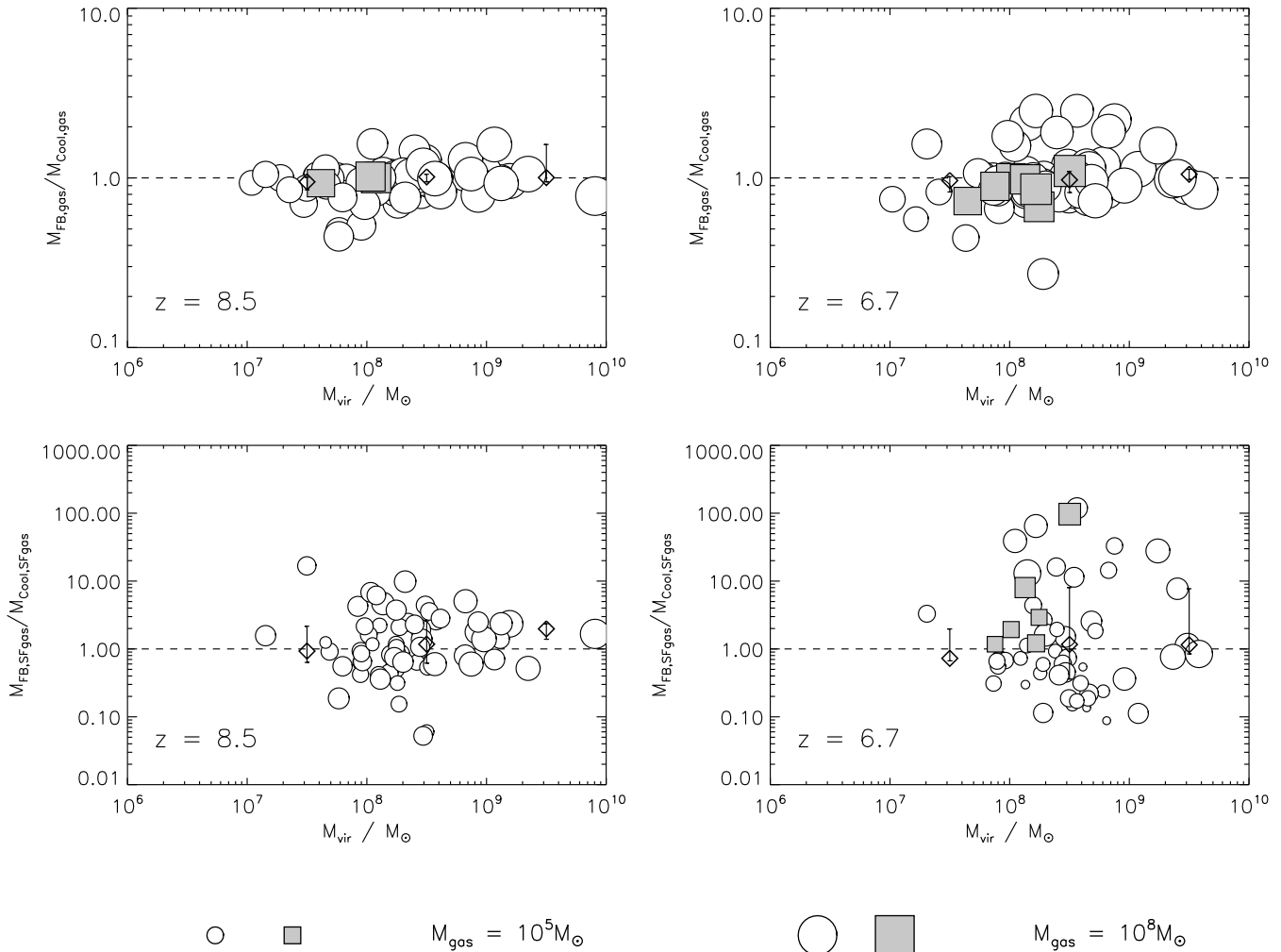


Figure 7. Ratio of gas mass in galaxies within r_{vir} in the Cooling and Feedback runs, plotted against the total halo mass of their twin halo in the Reference run. The figure shows galaxies at the redshift of reionization $z = 8.5$ on the left, and $z = 6.7$ on the right. The top plots show the ratio of total gas mass between runs, while the bottom plots show the ratio of the star-forming gas mass (i.e. $\rho > 10^5 \text{ atoms/cm}^3$). A grey square indicates that the halo of that galaxy survives as a Milky Way satellite at $z = 0$; white circles are halos that are completely disrupted by $z = 0$. The symbol size corresponds to the gas mass in the Feedback run inside that radius (see legend). We overplot as diamonds with error bars the median and interquartile range of the fractional differences in halo mass bins $10^7 M_\odot - 10^8 M_\odot$, $10^8 M_\odot - 10^9 M_\odot$ and $10^9 M_\odot - 10^{10} M_\odot$. The median values lie around the horizontal line marking an equal ratio, with the $10^7 M_\odot$ to $10^8 M_\odot$ bin having a ratio of ~ 0.95 and the higher mass bins having a 1:1 ratio or higher. There is a large amount of scatter in the relative amounts of star forming gas in halos in the two simulations. It is worth noting that some of the halos at each redshift sampled, including all of the Milky Way satellite progenitors at $z = 8.5$, do not contain star-forming gas. This is explained as star formation occurring in bursts, with the smaller galaxies containing no star-forming gas at certain instants in time.

that have already formed stars, it does not do so abruptly, but rather over a significantly extended period of time.

Another potential effect of reionisation is to quench galaxy formation by preventing the collapse of gas within halos that have not yet formed stars (e.g. Gnedin (2000); Somerville (2002); Benson et al. (2002)). However, the last $z = 0$ satellite galaxy to be formed in our Reference run begins forming stars at $z = 4.8$ in a halo with $M_{vir} = 1.4 \times 10^7 M_\odot$, and there are 9 other satellite galaxies hosted by halos with a similar mass which form their first star after $z = 8.5$. Hence, whilst it is still possible that UV photoionisation has a long-term role in preventing some galaxies from forming, it does not seem to be able to halt galaxy formation entirely.

In figure 10, we recast this statement in terms of minimal circular velocity for a star forming halo, v_{max} , below which halos are prevented from forming stars. This allows us to directly compare our results to those presented by Okamoto & Frenk (2009). As these authors, we cannot definitively conclude that this threshold arises entirely because of reionisation or the general inability of halos below a v_{max} of 10 km/s to cool and form stars by $z = 0$, since we do not run a simulation without reionisation. However, we note that reionisation in our simulation occurs instantaneously at $z = 8.5$ (close to the value of $z = 9$ of Okamoto & Frenk (2009)) and that, in stark contrast the threshold of $v_{max} \approx 10 \text{ km/s}$ seems independent of redshift. Indeed, it remains quite constant both before and after reionisation has oc-

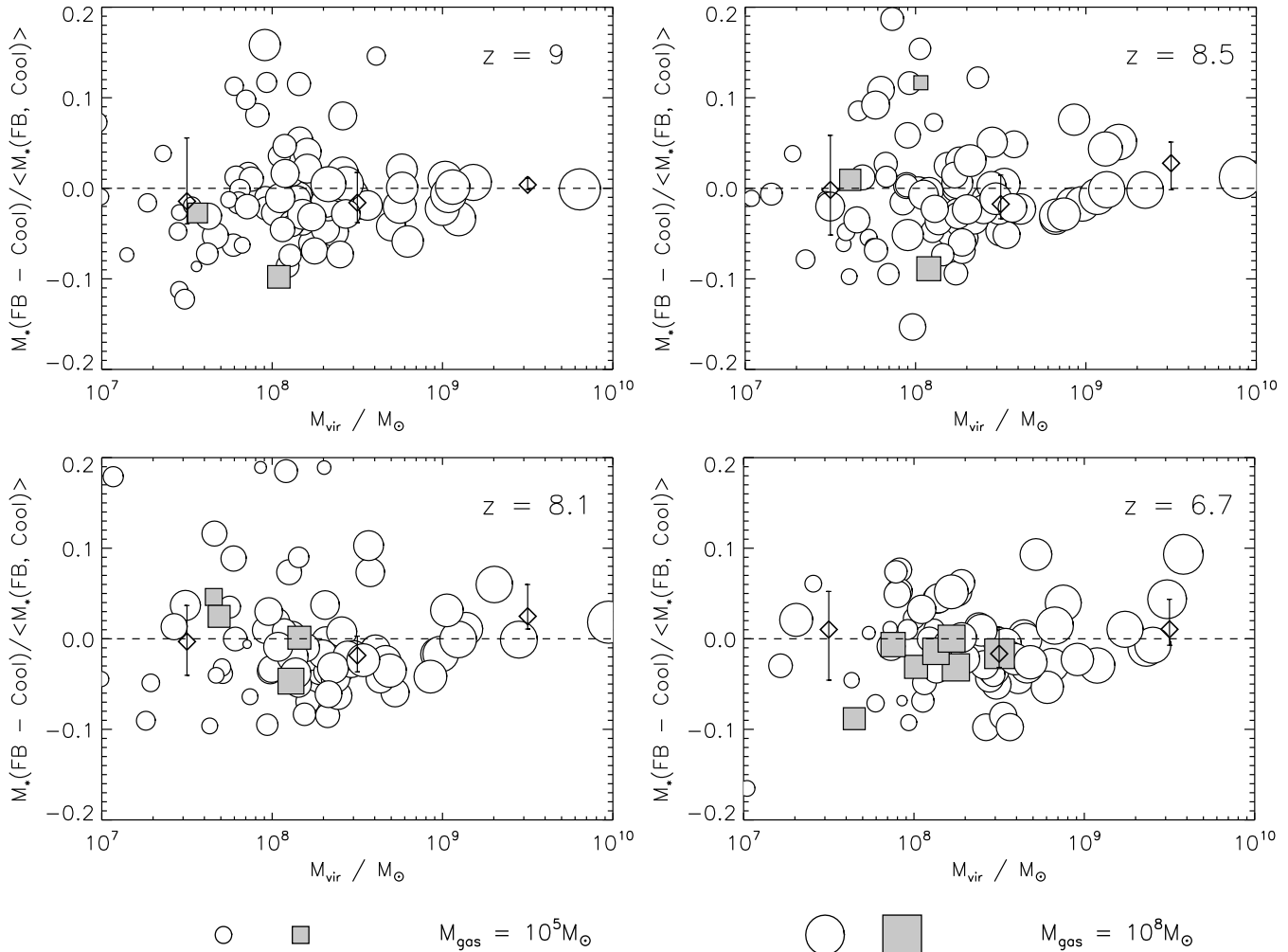


Figure 8. Fractional difference between stellar masses of galaxies in the Cooling and Feedback run $(M_{\star\text{FB}} - M_{\star\text{Cool}}) / (0.5(M_{\star\text{FB}} + M_{\star\text{Cool}}))$ versus total twin halo mass in Reference Run, where $M_{\star\text{FB}}$ is the stellar mass in the Feedback run and $M_{\star\text{Cool}}$ is the stellar mass in the Cooling run. A positive value indicates that the inclusion of supernova feedback enhances star formation in the given galaxy, while a negative value means that supernova feedback suppresses star formation. Different panels show the values for different output redshifts, from $z = 9$ (top left) to $z = 6.7$ (bottom right). The symbol size indicates stellar mass (see legend). Grey squares represent halos containing galaxies which survive as a Milky Way satellites at $z = 0$; a halo represented by a white circle is completely disrupted by $z = 0$. We overplot as diamonds with error bars the median and interquartile range of the fractional differences in halo mass bins $10^7 M_\odot - 10^8 M_\odot$, $10^8 M_\odot - 10^9 M_\odot$ and $10^9 M_\odot - 10^{10} M_\odot$. Star formation is slightly suppressed in low mass halos with weaker gravitational potentials. The trend is reversed for high mass halos.

curred, which leads us to argue that reionisation cannot play an important role in setting its level and only sustains it, in the best of cases.

4 MILKY WAY SATELLITES TODAY

4.1 Tracking satellite galaxies down to $z = 0$

In section 2.4, we discussed the techniques used to track the galaxies formed in the Cooling and Feedback run down to $z = 0$ using the Reference run. We now analyse the results of this tracking. The merger tree for the Reference run is shown in Fig. 11 where we track halos (marked as circles) becoming subhalos (marked as squares), and being tidally disrupted (squares become smaller) before completely merging with

their hosts. We resolve about 6630 such halos. Of these 6630, 394 survive as subhalos of the Milky Way halo at $z = 0$. In table 2, we list the number of galaxies formed by various redshifts from $z = 11$ to $z = 6.7$ in the Cooling and Feedback runs that survive to $z = 0$. It is apparent from the table that by this redshift, we have not formed enough satellite galaxies to match even the population of pre-SDSS satellites (Mateo 1998). However, it is also clear that satellite galaxy formation continues after reionisation; three galaxies that end up as satellites of the Milky Way at $z = 0$ are formed between $z = 8$ and $z = 6.7$.

In fact, we find that the youngest Milky Way satellite galaxy in the Reference run begins forming stars at $z = 4.8$, or a lookback time of 12.4 Gyr. This is illustrated on Fig. 12 where we plot the stellar mass of each Milky Way satel-

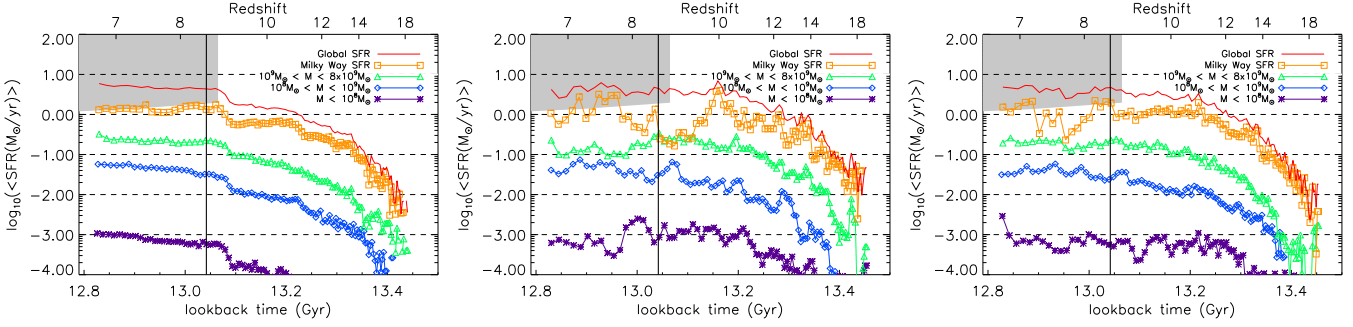


Figure 9. Mean star formation histories for different halo mass bins in the Reference run (left) Cooling run (middle) and Feedback run (right). Mean star formation rates (SFR) in M_{\odot}/yr are given for halos of mass $M < 10^8 M_{\odot}$ (purple asterices), $10^8 M_{\odot} < M < 10^9 M_{\odot}$ (blue diamonds) and $10^9 M_{\odot} < M < 8 \times 10^9 M_{\odot}$ (green triangles), as well as the Milky Way (orange squares) and the global SFR for the entire high resolution region (red solid line). The vertical line at $z = 8.5$ (look-back time 13.042Gyr) shows the point at which reionisation is turned on in the simulations. The grey region shows the detectable star formation rates as determined by Wilkins et al. (2011). This suggests that the SFR for a Milky Way-like galaxy progenitor is almost detectable at $z \sim 8$ (lookback time ~ 13.0 Gyr). We find no sudden drop in star formation in any mass bin after reionisation for any of the simulations. In fact, some of the star formation rates increase by up to 0.5 dex at reionisation. The jumps in star formation rates in the Reference run are due to the triggering of a new level of refinement on the grid, which allows the gas to collapse to allow star formation in all potentially star-forming regions (Rasera & Teyssier 2006).

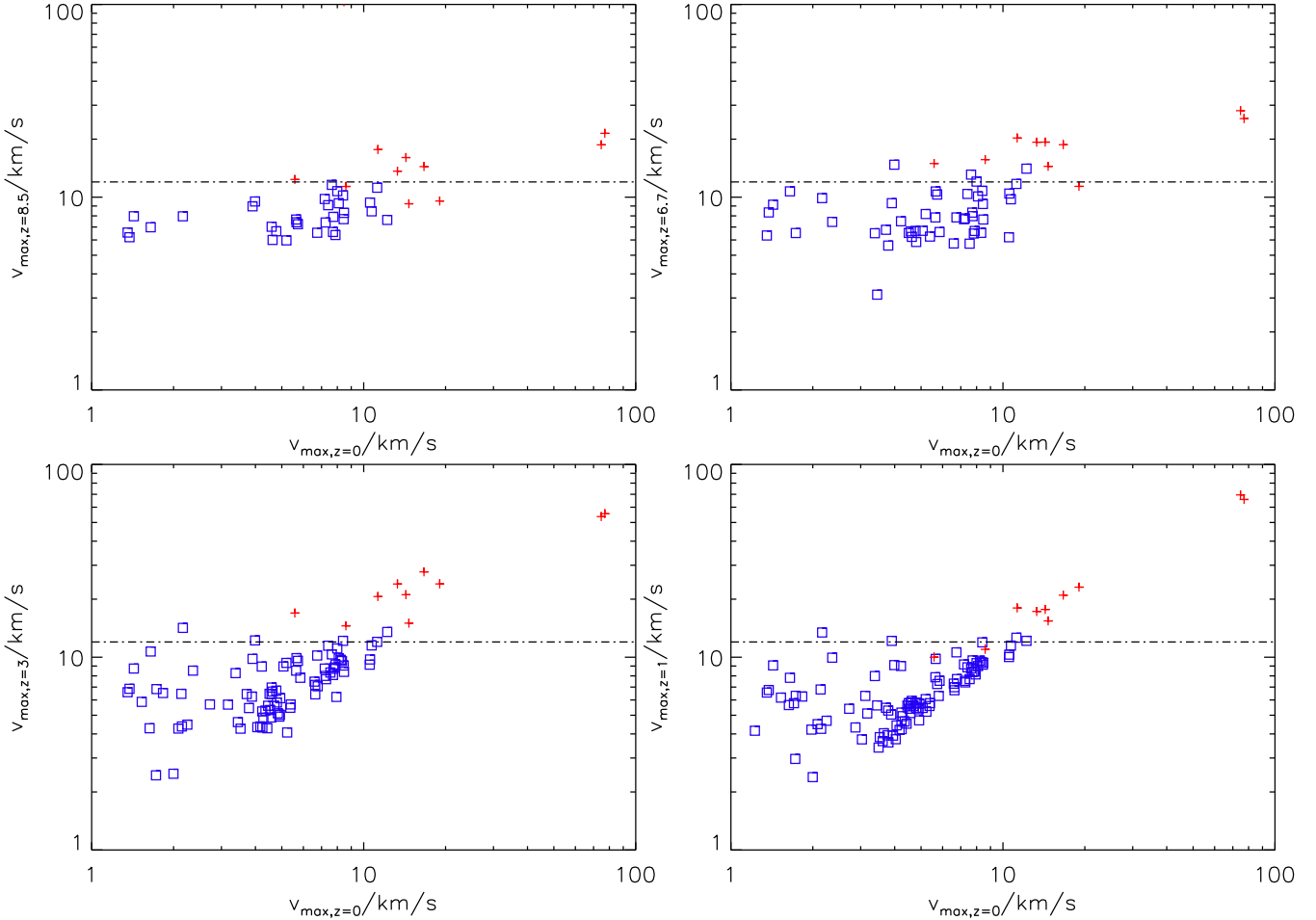


Figure 10. Maximum circular velocity of satellite halos at $z = 0$ versus the maximum circular velocity of their main progenitor at, from top left to bottom right, $z = 8.5$ (just prior to reionisation), $z = 6.7$, $z = 3$, $z = 1$. In red are the satellites that contain stars at $z = 0$ in the Reference run; the blue satellites remain dark. The dotted horizontal line is at 12km/s and represents the threshold given in Okamoto & Frenk (2009) above which halos can form stars before reionisation. Like these authors, we find halos that form stars under this threshold to about 10km/s; below this, no halos can form stars. Note that this threshold seems independent of redshift and that surviving Milky Way satellite galaxies begin to be captured by the Milky Way progenitor at $z = 3$. The halos with $v_{max,z=0}$ around 80km/s are satellites labelled ‘a’ and ‘h’ (see Fig. 5).

lite galaxy in the Reference run at $z = 0$ against the age of their oldest star particle. This figure shows that the youngest galaxies typically are the lowest mass galaxies. Since Fig. 4, further demonstrate that galaxies formed after a lookback time of 13.0 Gyr have ages that match well between the Reference and Feedback/Cooling runs, these results also are valid for the Feedback run. However, as we note in section 2.2, we are unable to identify galaxies with a stellar mass below $3.5 \times 10^5 M_\odot$ in the Reference run. Hence we cannot discount the possibility that the Cooling and Feedback runs might form more galaxies with lower masses that survive as Milky Way satellite galaxies. All we can conclude is that every galaxy above this mass threshold that survives as a Milky Way satellite in the Cooling and Feedback runs (through the twinning procedure) also survives as a satellite in the Reference run. However, it is possible that the trend of lower mass satellite galaxies forming at lower redshifts continues in the Cooling and Feedback runs, where stellar masses is better resolved.

Key to the survival process of satellite galaxies is the mass stripping they undergo as a function of time. We visualise this in Figs. 13 and 14 where we identify which halos containing stars at $z = 6.7$ survive to become Milky Way satellites at $z = 0$ and follow their dark matter and star particles through cosmic time. We locate these particles in outputs of the simulation at $z = 3, 1$ and 0 , and overplot them on top of their respective underlying density fields, colour coding them according to the redshift at which the halo they belong to is captured by that of the Milky Way. We find that halos captured before $z = 1$ experience significant disruption, with multiple tidal streams created despite the core of the halo surviving (halos ‘c’, ‘e’, ‘f’ and ‘g’ in Fig. 13). By contrast, the only stars formed by $z = 6.7$ that are stripped from their galaxies are from satellites captured before $z = 3$ (Fig. 14). The surviving satellite that is captured just after $z = 3$ (halo ‘g’) arrives in the Milky Way halo as a subhalo of another halo, which is subsequently disrupted by the Milky Way. Hence this halo has already experienced some stripping by $z = 3$, as shown in Fig. 13.

In Fig. 15, we investigate satellite survival to $z = 0$ in more detail. We compare the redshift at which a halo is captured by the Milky Way halo against its mass at capture in two simulations: the Reference run and the matching Adiabatic run. The only difference between these two runs is that an extra right hand side ‘sink’ term is included in the energy equation of the gas in the Reference run to model losses due to radiative cooling, as well as star formation (see section 2.1). We find that out of all the halos which survive to $z = 0$ in these two runs (6 in the Reference run, 20 in the Adiabatic run), only one is captured at $z > 3$ in the Adiabatic run and none in the Reference run. Moreover, higher mass halos ($M_{\text{vir}} > 10^9 \sim M_\odot$) only survive if they are captured later so that the highest mass satellites at $z = 0$ are systematically the ones that are captured last. This trend with mass is naturally expected since it is well known that dynamical friction makes massive satellites sink to the centre of their host halo faster than their lower mass counterparts (e.g. Binney & Tremaine (2008)). Whilst the Chandrasekhar formula described by these authors yields an incomplete picture of the interaction of satellites with their host (see e.g. Taylor & Babul 2001), one expects the trend in mass to persist in spite of tidal stripping and gravitational

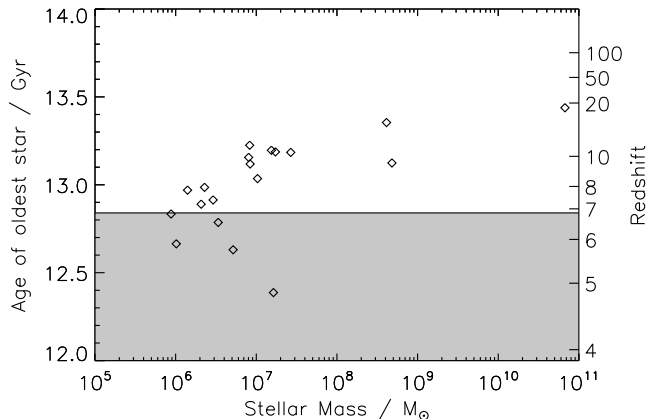


Figure 12. Time of first star formation for satellite galaxies that survive to $z = 0$ (including the MW itself) in the Reference run against their stellar mass at $z = 0$. The region shaded in grey represents the lookback times which have not been simulated in the high resolution Cooling and Feedback runs. This illustrates that satellite galaxy formation is incomplete until $z = 4.8$ (i.e. after a lookback time of 12.4 Gyr). Note that this plot only shows galaxies in the Reference run.

heating. However, what is perhaps more surprising is the relatively large impact that simply including radiative cooling has on the survival time of satellites. Indeed, we find that number of satellites which survive is dramatically reduced in the Reference run (from 20 objects in the Adiabatic run down to 6), which follows a similar trend to that described by Romano-Diaz et al (2010) when comparing identical simulations with baryons (and cooling) to their pure dark matter counterparts. This is explained by two effects: (i) it is more difficult to strip mass from satellites as their central density increases and (ii) the cuspsiness (and central density) of the host halo is increased. It is interesting to note that effect (i) could in principle lead to the opposite effect, i.e. an increase in the lifetime of the satellites as it makes them more concentrated and thus more resistant to tidal disruption, but we find that reduction in dynamical friction time scales due to mass increase dominates. Of course these conclusions could be altered if a substantial mass of baryons was ejected out of the satellites, to the point where the trend that we measure could even be reversed. Pontzen & Governato (2012) argue that such a reversal is plausible, though it would require a significantly more efficient feedback mechanism than the one we observe in section 3.1.

4.2 Dark Matter Satellite Halos

In this section, we consider the population of dark matter subhalos of the Milky Way in our runs at $z = 0$, comparing and contrasting their properties with similar dark matter simulations which exist in the literature.

For this purpose, we run a fourth simulation, the Dark Matter run, which is identical to the Cooling and Feedback runs except that the mass in baryons is replaced with dark matter mass, such that a dark matter particle is $1/(1 - f_b)$ times the mass of a dark matter particle in the Cooling and Feedback runs (see section 2.1). This simulation is described in more detail in section 4.3. We use it to compare our results directly with the Aquarius (Springel et al. 2008) and

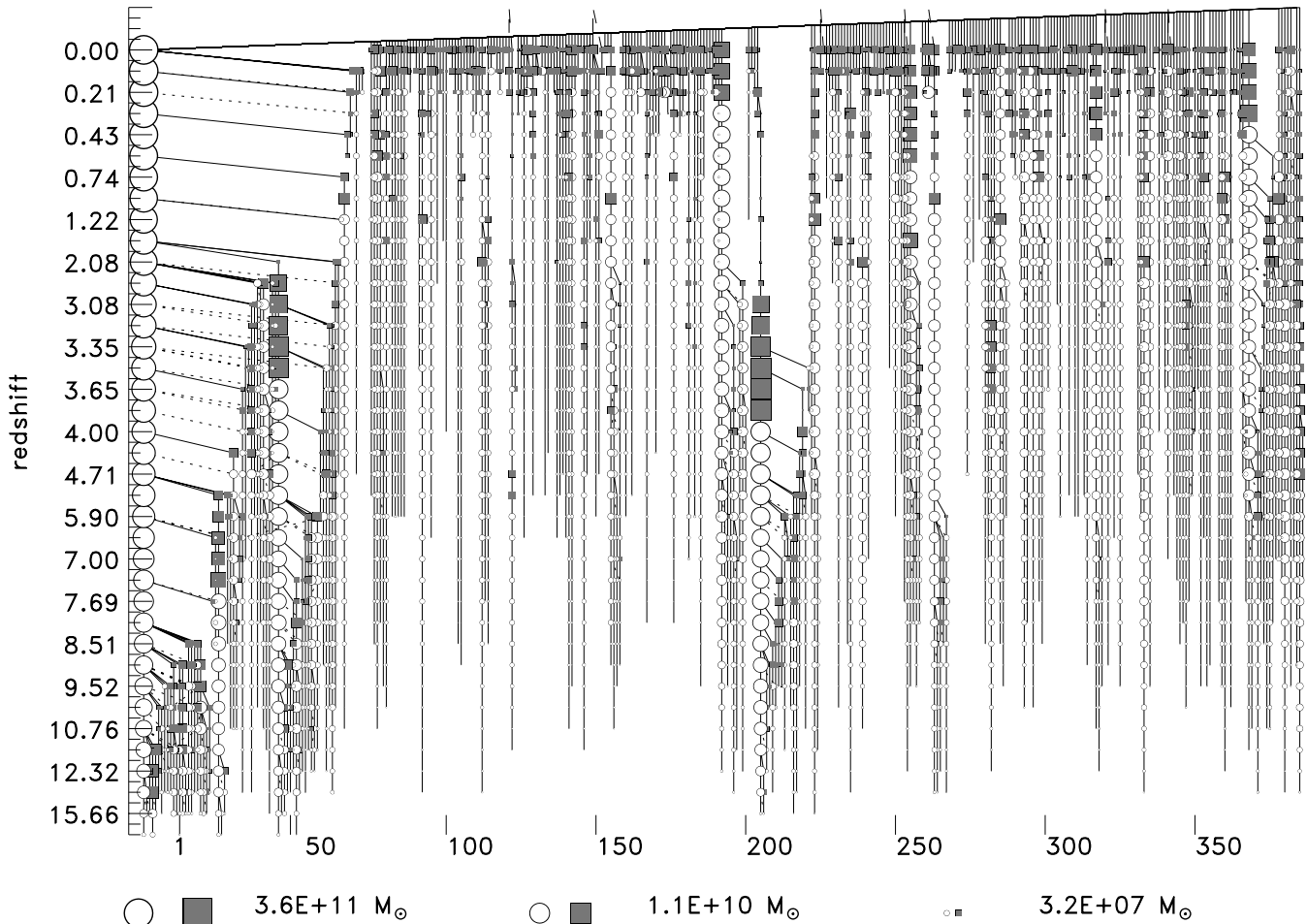


Figure 11. Halo merger tree for our Milky Way-like galaxy from $z = 15.6$ to $z = 0$ in the Reference run. We only show the most massive branches of the tree on the figure, because in total, we find 6630 branches, of which 394 survive down to $z = 0$. The left-most branch represents the mass evolution of the Milky Way halo itself. White circles represent independent halos; grey squares represent subhalos. Symbol size is proportional to dark matter halo mass; see the legend for values. Solid diagonal lines represent final mergers with the host, and vertical lines represent the time evolution of an individual halo. Dashed diagonal lines indicate when a halo becomes the subhalo of another halo. To the right of the plot (branch numbers > 70) are the most massive branches which reach $z = 0$.

Via Lactea II (Diemand et al. 2008) simulations, which are the most resolved dark matter only simulations of MW-like objects available to date. The most basic comparison, a cumulative maximum circular velocity function, is presented in Fig. 16. In this figure, we also overplot the empirical prescription proposed by Reed et al. (2005) for the Milky Way halo in our Dark Matter run at $z=0$. We find that our Dark Matter run satellite halo data is well represented by this prescription, but that the Reference run predicts significantly fewer satellites at the low velocity end (between a factor 2 and 3 for $V_{max} < 20\text{km/s}$), and more massive satellites ($V_{max} > 30\text{km/s}$). We discuss the impact of simulation physics on the maximum circular velocity function in the next section (4.3).

From Fig.16, it is apparent that, whilst the cumulative maximum circular velocity function of our Dark Matter run has the same shape ($N(> V_{max}) \propto V_{max}^{-3}$) as that measured in both the Aquarius and Via Lactea II simulations, its normalisation is more than an order of magnitude lower. This large discrepancy can almost entirely be attributed to our choice for the mass of the MW host halo

since our agreement with the Reed et al. (2005) prescription is quite reasonable (better than 20 %). Springel et al. (2008) report that their simulations overshoot the fitting formula of Reed et al. (2005) by a factor ~ 3 which they argue most likely arises from a systematic effect in the numerical technique used to perform the runs. On the other hand, Madau et al. (2008) suggest it is due to the different (WMAP 1 instead of WMAP 3/5/7, i.e. different normalisation, σ_8 , and/or tilt, n_s , of the power spectrum) cosmology the Aquarius simulations employ. In any case, the remarkable conclusion that we draw from this comparison exercise, is that for a MW host halo with $V_{max}=126\text{ km/s}$ in the Dark Matter run as opposed to $\approx 210\text{ km/s}$ in the Aquarius or VLII simulations, i.e. a difference of about 65 %, one gets a suppression in the number of satellites by about a factor of 10, which is enough to match the observed abundance of MW satellites with V_{max} between 10 and 30 km/s. Now, there is still an ongoing debate as to what the exact mass of the Milky Way halo is (e.g. Battaglia et al. (2005); Karachentsev & Kashibadze (2005); Watkins et al. (2010)). Our simulated halo admittedly lies at the very low end of

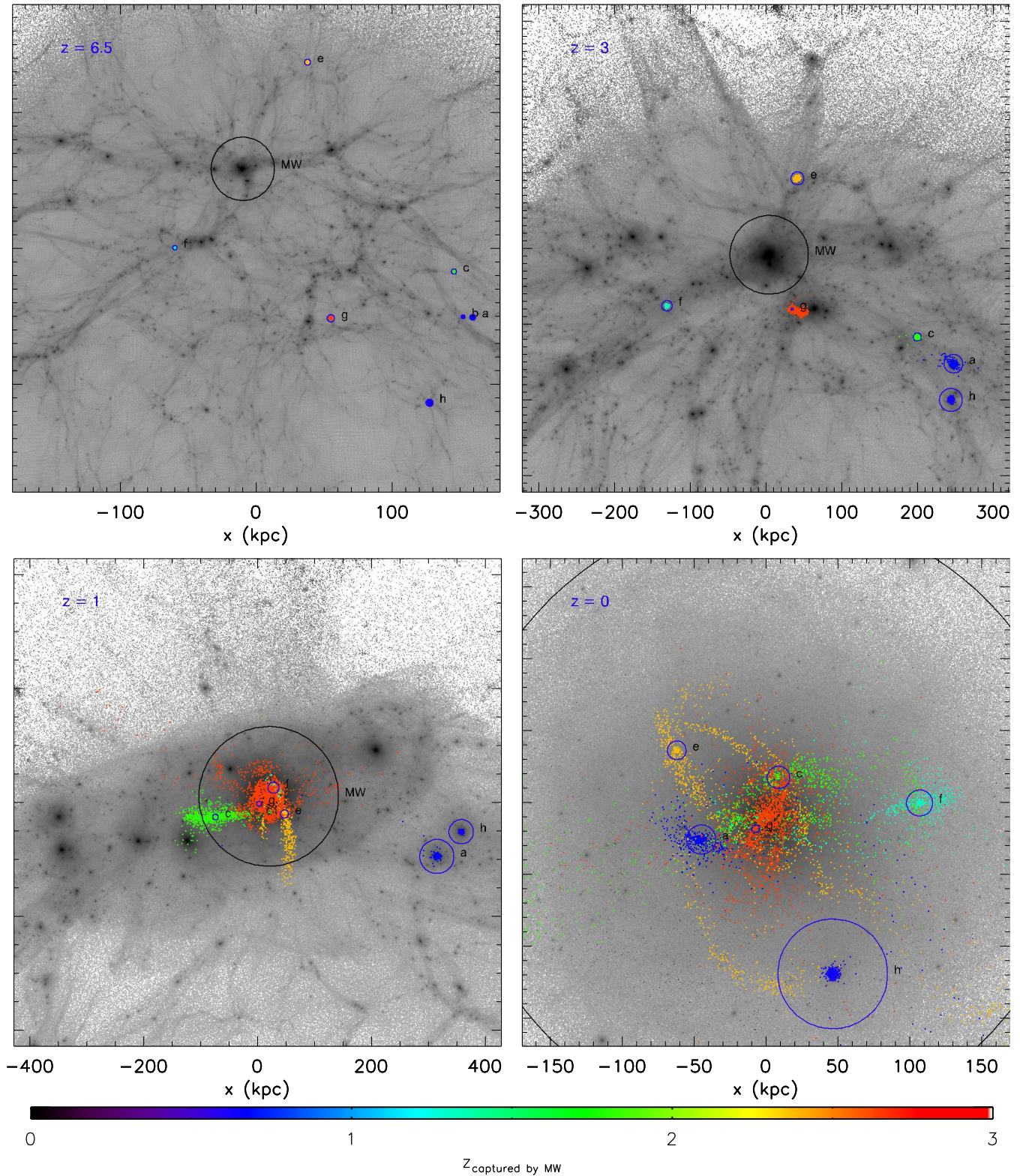


Figure 13. Tracking the location of dark matter particles in MW satellite progenitor halos from $z = 6.7$ to $z = 0$ in the Reference run. Each image is a projection of a cubic volume of length shown on the x-axis in physical kpc. Blue circles represent the virial radius of each halo tracked; the MW halo is shown as a black circle. The image at $z = 0$ lies largely inside the Milky Way virial radius. The colour of the particles in a halo represents the redshift at which the halo is captured and becomes a subhalo of the MW (see the colour bar). Halos captured before $z = 1$ exhibit significantly more stripping at $z = 0$ than halos captured after $z = 1$. The dark orange halo (halo ‘g’ in figure 5) is captured and partially stripped by another halo which, in turn, is captured and completely disrupted by the Milky Way between $z \leq 3$ and $z = 1$, while halo ‘g’ itself survives as a luminous satellite galaxy of the MW at $z = 0$.

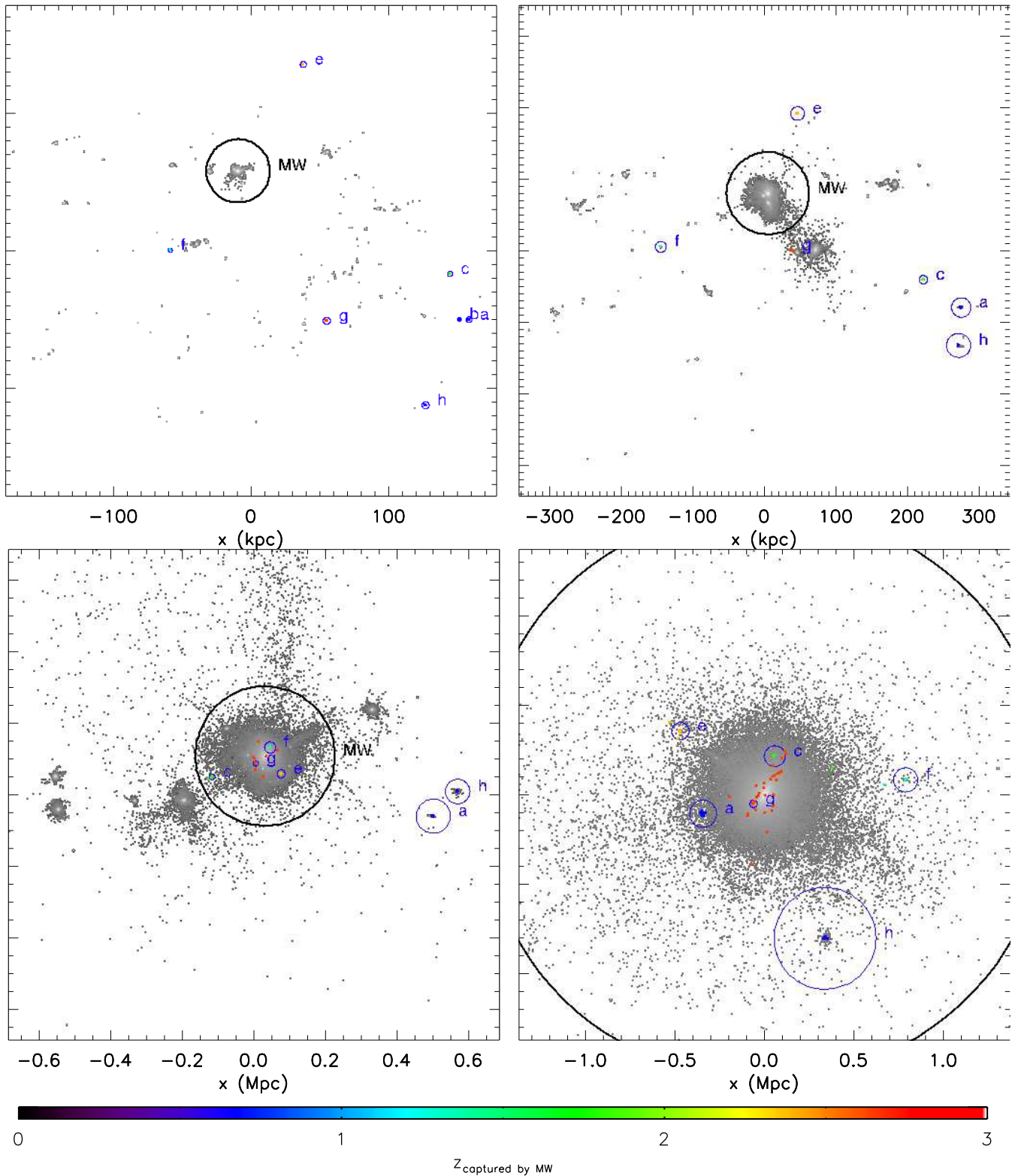


Figure 14. Tracking the location of star particles in MW satellite progenitor halos from $z = 6.7$ to $z = 0$ in the Reference run. As in Fig. 13, each image is a projection of a cubic volume of length shown on the x-axis in physical kpc and circles indicate virial radii. The background greyscale indicates the stellar column density. The colour of the particles in a galaxy represent the redshift at which the galaxy is captured and becomes a satellite of the MW (see the colour bar). With the exception of galaxies captured by the MW around $z \leq 3$ ('e', 'f' and especially 'g'), which form stellar streams around the MW centre, most stars formed before $z = 6.7$ remain part of their host galaxy.

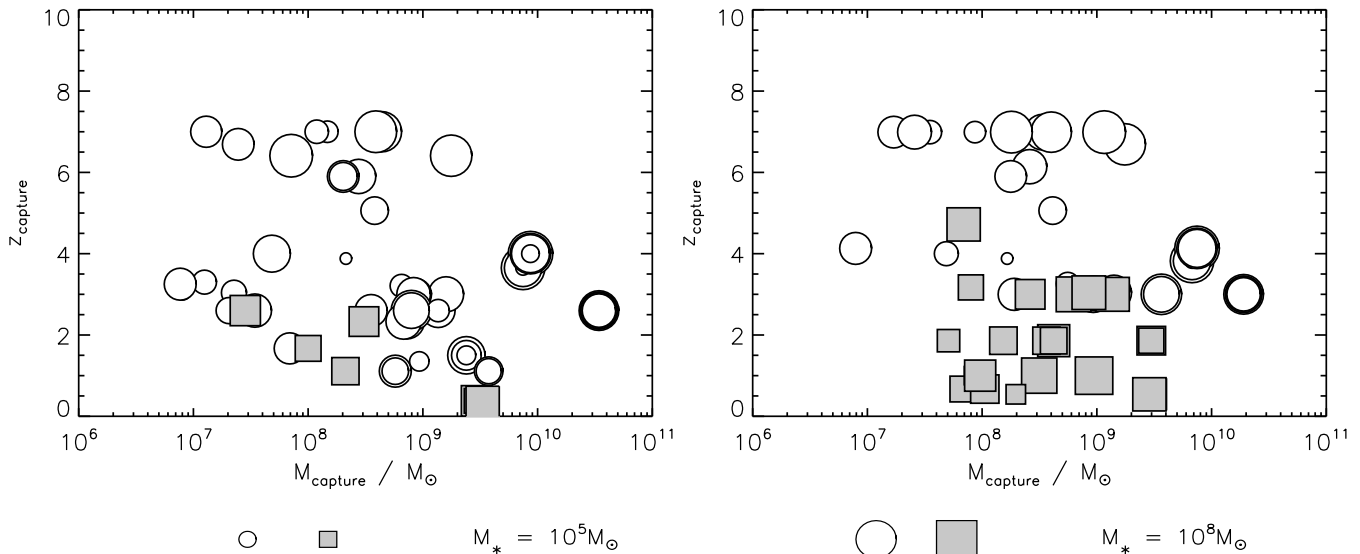


Figure 15. Survival of halos as MW satellites at $z = 0$. Both panels show the redshift at which a halo becomes a MW sub-halo, z_{capture} , against the sub-halo mass when this capture happens, M_{capture} ; on the left is the Reference run, and on the right is the Adiabatic run. The symbol sizes represent the stellar mass of the galaxies hosted by each halo twinned in the Feedback run at $z = 6.7$ (see legend on the figure). Grey squares survive as MW satellite halos at $z = 0$. Note that they can be completely disrupted as long as they become part of another MW satellite halo by $z = 0$ in the disruption process. White circles are completely disrupted and simply become part of the diffuse MW halo by $z = 0$. Any symbol which completely overlaps with another represents a sub-halo that has been completely disrupted by its host halo before its capture by the MW halo, forming a single object at the time of capture. Halos captured by the MW host before $z = 3$ do not survive to $z = 0$, with one exception in the Adiabatic run. Only a small fraction of the low-mass halos ($M_{\text{vir}} \leq 10^9 M_{\odot}$) captured after $z = 3$ are able to survive to $z = 0$ in the Reference run, whereas the vast majority of them survive in the Adiabatic run.

the estimated range of values ($4.32 \times 10^{11} M_{\odot}$ within 195 kpc), and Aquarius and Via Lactea II somewhat on the high side ($1.85 \times 10^{12} M_{\odot}$ within 245 kpc). It is not the purpose of the present paper to create new constraints Milky Way halo mass or to argue which mass is more realistic, but only to illustrate how the uncertainty in the mass of the Milky Way halo and the inclusion of baryonic physics translate into an uncertainty in the number and properties of MW satellites one predicts. Thus we simply remark that the observed abundance of these satellites, taken at face value, seems to favour a light MW halo.

4.3 The Effect of Baryonic Physics on Satellite Galaxy Survival

In this section we discuss the effect of the baryonic physics included in the Reference run on the survival of satellite galaxies to $z=0$. Various authors have investigated the issue by running SPH galaxy simulations and comparing them to identical simulations in which the gas particles in the initial conditions are removed and their mass added to the dark matter particles, as we do in our Dark Matter run. For instance, Peirani (2010) adopts this strategy to study the Hubble flow on Mpc scales. He finds that the peculiar velocities of independent halos match well between simulations and that a cut in the maximum halo circular velocity of 30km/s in the pure dark matter run yields an excellent match with the halos containing galaxies in the baryonic run. Hence he concludes that for independent halos, predictions of which halos contain galaxies are robust. By contrast, we

find that the baryonic physics included in our high resolution re-simulation of a MW class halo has a dramatic effect on the number of satellite galaxies it possesses at $z = 0$.

As described in section 2.1, we run three simulations to $z = 0$. The first one is the Dark Matter run. This is a pure N-body simulation, in which the mass in baryons corresponding to Ω_B is replaced by an equivalent increase in dark matter mass (note that in this case, RAMSES solves the Poisson equation using an AMR grid refined according to the same quasi-Lagrangian refinement criteria applied to dark matter alone (Teyssier 2002)). The second simulation is the Adiabatic run. This simulation is identical to the Dark Matter run, except that it now contains the universal baryon mass fraction and solves the Euler-Poisson equations to follow gas dynamics. However, contrary to the third simulation, the Reference run, gas in the Adiabatic run is not permitted to cool radiatively. Star formation is also omitted in this run, though a Haardt & Madau (1996) UV background is included to minimise differences with other baryonic runs. Finally, to extend our analysis to runs with higher resolution (Cooling run) and including more detailed physics (Feedback run), we use the technique described in section 4.1 to predict the number of luminous halos at $z = 6.7$ that survive to $z = 0$.

The first thing to note is that the Dark Matter run produces more (sub-)halos ($\approx 20\%$ more) than any of the runs containing baryons; we present exact numbers in table 3. This difference is attributed to gas pressure delaying/suppressing halo collapse. Indeed, the collapse of purely collisionless dark matter halos is unimpeded by pressure

High z	Simulation	Total Number high z (twinned)	Total Number $z = 0$	Satellite Mergers Destroyed (high $z \rightarrow z = 0$)	Merged with MW (high $z \rightarrow z=0$)
11	Cooling	66 (36)	1	0 (0 \rightarrow 0)	65
	Feedback	65 (35)	1	0 (0 \rightarrow 0)	64
	Reference	36 (36)	0	0 (0 \rightarrow 0)	36
9	Cooling	91 (61)	2	0 (0 \rightarrow 0)	89
	Feedback	89 (60)	2	0 (0 \rightarrow 0)	87
	Reference	63 (63)	1	0 (0 \rightarrow 0)	62
8.5	Cooling	89 (71)	3	0 (0 \rightarrow 0)	86
	Feedback	89 (71)	3	0 (0 \rightarrow 0)	86
	Reference	77 (77)	2	0 (0 \rightarrow 0)	75
8	Cooling	82 (68)	3	1 (2 \rightarrow 1)	78
	Feedback	90 (73)	3	1 (2 \rightarrow 1)	86
	Reference	85 (85)	4	0 (0 \rightarrow 0)	81
6.7	Cooling	85 (78)	6	1 (2 \rightarrow 1)	78
	Feedback	85 (79)	6	1 (2 \rightarrow 1)	78
	Reference	107 (107)	7	1 (2 \rightarrow 1)	99

Table 2. Table of the fate of galaxies formed between $z = 11$ and $z = 6.7$. The 6 columns are, from left to right: (1) the redshift at which the stellar population is sampled in the Reference, Cooling and Feedback runs (‘high z ’); (2) the simulation name; (3) the number of galaxies which become satellites of the MW between the sampled redshift and $z = 0$ not including the main MW progenitor halo (in brackets, the number of those galaxies whose twin halos in the Reference run also contain at least a galaxy); (4) the number of galaxies surviving as MW satellites at $z = 0$; (5) the satellite progenitors destroyed by mergers with other satellite progenitors - the figures in brackets show the number of objects taking part in mergers at high z , followed by the resulting number of objects after the satellite progenitor-satellite progenitor mergers at $z = 0$; (6) the number of galaxies merged with the MW and destroyed between high z and $z = 0$. See section 2.4 for a description of how these numbers are calculated. We find that the large majority of the halos containing galaxies captured by the MW by $z = 0$ merge with it and are destroyed, with two galaxies merging with each other before being captured by the MW and becoming a satellite galaxy. More mergers of MW progenitor galaxies are found, but these are all completely disrupted and destroyed after capture by the MW. We find that satellite galaxy formation in the Reference run is not complete by the lowest redshift reached by the high resolution runs ($z=6.7$). By looking at the ages of the star particles in satellite galaxies at $z = 0$ in the Reference run, we find that satellite galaxy formation continues until at least $z = 4.8$ (see Fig. 12).

Redshift	Halo Type	Dark Matter	Adiabatic	Reference	Cooling	Feedback
0	Independent Halos	2084	1706	1731	-	-
	Subhalos	2730	2418	2209	-	-
7	Independent Halos	2405	1997	1997	2142	2104
	Subhalos	598	449	343	445	390

Table 3. Total number of independent halos and subhalos (dark and luminous) in the Dark Matter, Adiabatic and Reference runs at two sampled redshifts. Runs containing baryons compare favourably, whereas the Dark Matter run contains significantly more halos for a given redshift. We attribute this to the effect of pressure in baryons resisting gravitational infall. Dark matter particles do not experience this and are able to collapse more easily into halos under gravity. There are also fewer subhalos in the Reference run than either of the other two runs, as explained in section 4.3.

forces. This effect is roughly independent of redshift. Secondly, we find fewer subhalos in the Reference run than in the two other runs. Figure 17 shows that the total (gas & DM) density profiles of the main MW halo at $z = 0$ are very similar between the DM and Adiabatic runs, with the Adiabatic run having a slightly lower density overall. However, gas in the Reference run is able to cool, and hence the density of the halo within a radius of 10kpc is significantly higher in this run, since cooled baryons are able to condense at the centre, pulling DM along with them Flores & Primack (1994). This higher central density plays an important role in destroying subhalos, and hence satellite galaxies: as mentioned in section 4.2, the Reference run subhalo cumulative maximum circular velocity function lies below the Dark Matter run’s (figure 16).

In figure 18, we further quantify this effect by plotting the number of high redshift galaxies surviving to become

satellite galaxies of the Milky Way at $z = 0$ (see sections 2.4 and 4.1 for details on the tracking of satellites from high to low redshift and table 2 for numbers specific to the Reference run). We find that the Reference run contains far fewer (factor 3 to 7 depending on redshift) surviving satellite galaxy sub-halo hosts than the Dark Matter or Adiabatic runs. We attribute this quite dramatic difference to the stronger dynamical friction on satellites in the central region as this drag force scales proportionally to the host halo density (Binney & Tremaine 2008). Finally, we note that none of the satellite galaxies at $z = 0$, in any of the simulations, were captured by the Milky Way progenitor halo at $z > 3$; all galaxies captured by the Milky Way progenitor halo at redshifts higher than $z = 3$ are destroyed. However, in the Adiabatic run, all halos captured at $z < 3$ survive as subhalos down to $z = 0$, as opposed to the Reference run, where only a small fraction of them survives (see figure 15).

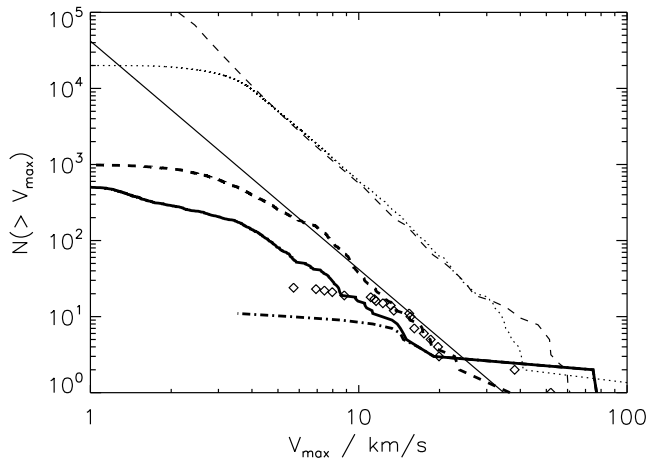


Figure 16. Cumulative maximum circular velocity (V_{max}) functions comparing our results to high resolution dark matter only simulations of MW-like objects at $z = 0$ published in the literature. The Reference run data is shown as a thick solid line, and the Dark Matter run as a thick dashed curve. Via Lactea II (VLII) data (Diemand et al. 2008) is overplotted as a thin dotted curve. A fit to the Aquarius data (Springel et al. 2008) is plotted as a thin dashed line. The empirical formula for $N(< V_{max})$ given by Reed et al. (2005) is plotted as a thin solid line. Observational data from Mateo (1998); Bekki & Chiba (2005); Bekki & Stanimirović (2009); Wolf et al. (2010) is shown as diamonds. In each case, V_{max} is given by $\max(\sqrt{GM(< r)}/r)$, where M is the mass inside r_{50} , the radius at which the density exceeds $50\rho_{crit}$. Our host halo has a V_{max} of 126km/s in the Dark Matter run as opposed to ~ 200 km/s in the Aquarius or VLII simulations. Note that we plot all subhalos inside r_{50} (denoting the radius at which the density is above $50\rho_{crit}$) as opposed to r_{200} , which we use in the rest of this paper. This is to allow comparison with Reed et al. (2005); Diemand et al. (2008); Springel et al. (2008). The Dark Matter run is reasonably well described by the Reed et al. (2005) formula indicating that the difference between our simulation and the Aquarius and VLII simulations are largely due to the MW host halo in the Aquarius and VLII having higher maximum circular velocities. By contrast, the Reference run lies below the empirical formula, which we comment on in section 4.3.

Our finding that gas cooling reduces the number of surviving satellite galaxies seems to run counter to Libeskind et al. (2010), who claim that gas cooling allows satellite halos to survive longer. However, Romano-Díaz et al. (2010, 2009); Schewtschenko & Macciò (2011) (also running Smoothed Particle Hydrodynamics (SPH) simulations like Libeskind et al. (2010)) reach the opposite conclusion (in agreement with ours), arguing that sub-halos survive a shorter time when gas cooling is included. It is worth pointing out that these studies all use tree-SPH methods as opposed to the AMR technique we use to model the self-gravitating baryon and DM fluid. Beyond the documented inability of the standard implementation of SPH to properly capture hydrodynamical instabilities (Agertz et al. 2007; Mitchell et al. 2009, e.g.), which is likely to cause an underestimate of the amount of gas stripped from satellite galaxies as they plough through the hot diffuse medium of their host halo, the main difference between the two numerical approaches lies in their estimate of the gravitational force. Indeed, whilst this force in Libeskind et al. (2010) is computed using a tree method which involves di-

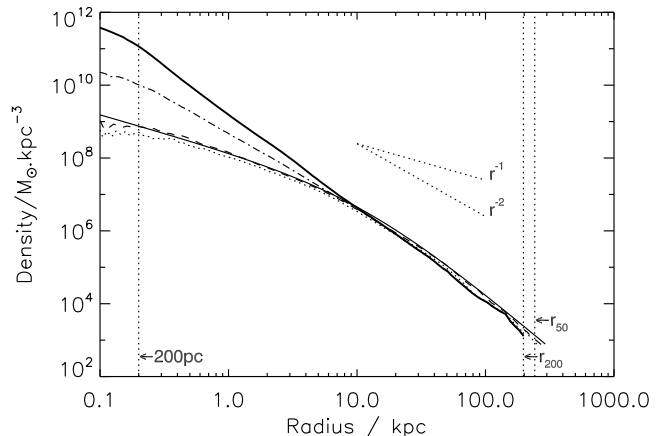


Figure 17. Density profiles of the main Milky Way-like halo up to r_{vir} at $z = 0$ for the Reference (thick solid line), Adiabatic (dotted line) and Dark Matter (dashed line) runs. We plot total density, i.e. dark matter, gas and stars except for the dot-dashed line which represents the DM density in the Reference run. We overplot a vertical dotted line at 200pc, equivalent to AMR level 16 at $z = 0$, i.e. 2 levels below the highest resolution reached by the runs to indicate the scale below which the gravitational force is underestimated, and lines at r_{200} , used in the bulk of the text and r_{50} , used for comparison purposes with figure 16. Power law profiles scaling like r^{-1} and r^{-2} and a NFW profile fit to the DM run (thin solid line) are also overplotted. The density profile in the Reference run departs from the others at 10kpc, and is several times higher at 2kpc. There is little noticeable difference between the Dark Matter and Adiabatic run density profiles. The high central density in the Reference run is due to gas cooling, and dramatically increases the stripping of sub-halos that pass in the central region of the halo. This effect is noticeable in figure 18, where the number of surviving satellite galaxies in the Reference run is dramatically lower than the number found in the Adiabatic and Dark Matter runs.

rect particle summation and a constant softening on small scales (Springel 2005, e.g.), Teyssier (2002) solve the Poisson equation on the AMR grid, i.e. with an adaptive softening directly linked to the grid cell size. Such a difference naturally leads to a better force resolution of the tree method in low density regions. However, the situation is reversed in high density regions typical of virialised halos, where the size of an AMR cell can become significantly smaller than the constant softening length used by tree methods. In our case, we reach a spatial resolution of ≤ 50 pc in the central region of the Reference run MW halo, which is significantly smaller than the values reported in the aforementioned SPH studies (several hundred parsecs deduced from fig 4 of Romano-Díaz et al. (2010), $500 \text{ h}^{-1} \text{ pc}$ quoted in Schewtschenko & Macciò (2011), and $150 \text{ h}^{-1} \text{ pc}$ in Libeskind et al. (2010)). This, in conjunction with a similar (or better) DM particle mass resolution as that reported in these studies, makes us quite confident that the force resolution achieved in the Reference run should not lead to a premature destruction of sub-halos, but allow them to better survive tidal disruption. Since we do not perform a tree-SPH counterpart to our AMR simulation using identical initial conditions, it is difficult to comment more quantitatively on the differences in number of satellites destroyed by these different techniques. However, we refer the interested reader to Schewtschenko & Macciò (2011) for a discussion of the pos-

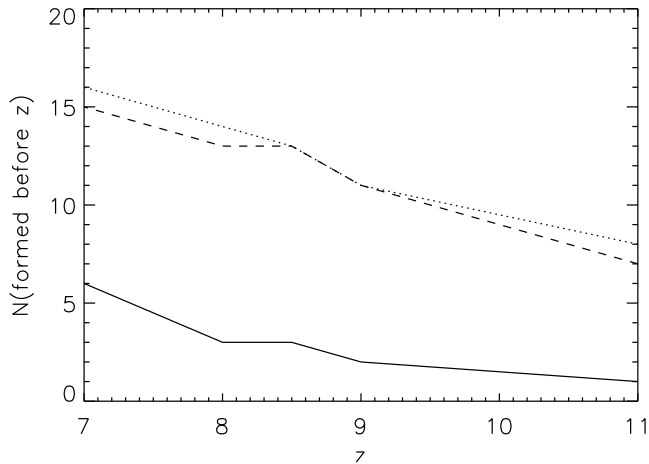


Figure 18. Number of satellite galaxies at $z = 0$ formed at or before a given redshift. Satellite galaxies are defined as sub-halos whose progenitors at high redshift have a twin in the Feedback run that contains one or more galaxies (see section 4.1). Each line represents a different run used to track halos down to $z = 0$. The solid line shows the Reference run, the dashed line shows the Dark Matter run and the dotted line shows the Adiabatic Run. The inclusion of gas cooling reduces the number of galaxies at high redshift that survive down to $z = 0$ by a factor ~ 3 to 10 depending on redshift. As discussed in the text, the central density profile of the Milky Way at $z = 0$ plays a key role in governing the survival of satellite galaxies.

sible reasons behind the discrepancy between their results and the results of Libeskind et al. (2010).

To conclude, even if our sub-halos had exactly the same mass in the DM and Reference runs, a higher density of the host halo would cause their orbits to decay faster, thus decreasing their survival time. This effect is exacerbated as the satellites in the Reference run are also more concentrated and therefore retain more mass on their way to the centre of the host as this renders them less prone to tidal disruption. We believe that the main caveat of our Reference run is that it does not include a feedback model. Indeed, Pontzen & Governato (2012) have recently argued that the injection of energy from supernovae in the centre of dwarf galaxies at $4 > z > 2$ can dramatically alter their halo density profiles. Whilst we are not able to confirm this effect with our own set of simulations, should it prove to be able to lower the central density of the Milky Way halo as well, we predict that more satellites will survive to $z = 0$. However, whether this number will match that measured in pure DM simulations or will still reflect a significant suppression of satellites is likely to depend on the details of the numerical implementation of the feedback processes.

4.4 Properties of Satellite Galaxies at $z = 0$

In this section we compare the properties of galaxies found at $z = 0$ in our simulations to observations of known satellite galaxies of the Milky Way and M31. To do this, we make use of the Reference run results measured at $z = 0$ directly rather than relying on the satellite tracking algorithm described in section 4.1. In this run, we find fifteen satellite galaxies using a direct galaxy identification method described in section 2.2. Four of these (labelled *i*, *l*, *r* and

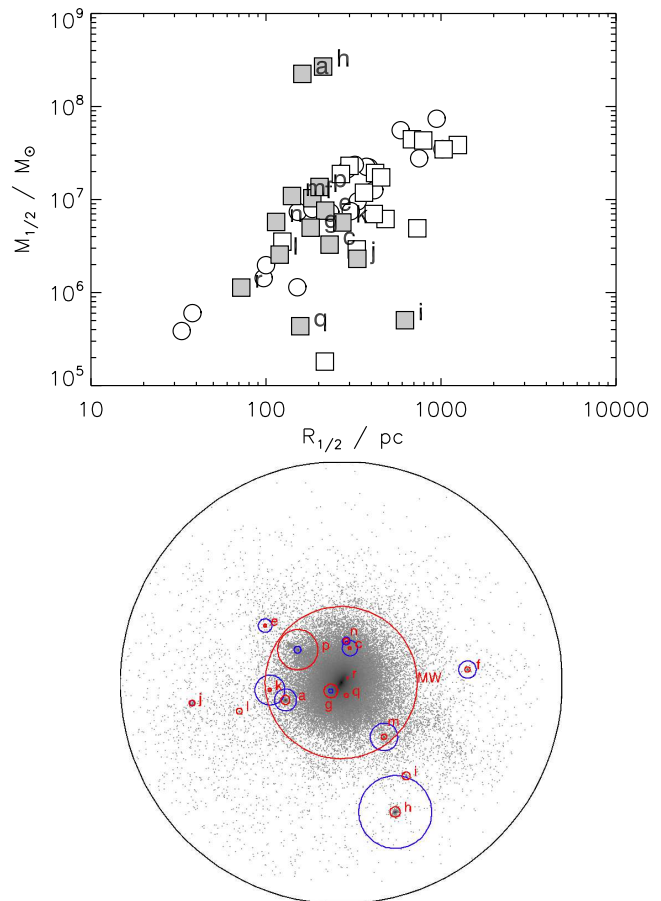


Figure 19. Properties of satellite galaxies surviving down to $z = 0$. The top panel shows half stellar mass against half-light radius for satellite galaxies in the Reference run at $z = 0$ (grey squares), compared to values calculated for satellites of the Milky Way and M31 (white circles and white squares respectively). Data for the satellites of the Milky Way are taken from Wolf et al. (2010). Data for the satellites of M31 are derived from Collins et al. (2011, 2010); Ferguson et al. (2000); Irwin et al. (2008); Irwin & Collins (2011, priv. comm.); Kalirai et al. (2010); Letarte et al. (2009); Martin et al. (2009); McConnachie et al. (2008); Morrison et al. (2003); Pustilnik et al. (2008); Richardson et al. (2011). The bottom panel shows the spatial location of the satellite galaxies and their host DM sub-halos inside the Milky Way virial radius (red circles indicate galaxy radii, while blue circles represent sub-halo radii). The black circle marks the Milky Way virial radius. The two satellite galaxies (labelled *a* and *h*) which lie above the observed data in the top panel are galaxies that have been little affected by stripping due to their late capture by the Milky Way host. Note that the Milky Way data does not include the Magellanic clouds or ultrafaint satellites.

q on Fig. 19) do not have associated dark matter host halos identified by our halo detection algorithm. Since these are the least massive satellite galaxies, this has two likely origins: (i) either the number of dark matter particles constituting the host sub-halo falls below the minimum number for detection as the outer regions are tidally stripped by the host, in which case the lack of dark matter host is simply the result of lack of mass resolution; (ii) or as pointed out by e.g. Knebe et al. (2011) since our halo finder does not consider particle velocities, sub-halos close to the centre of the host (*r* and *q* for instance in our case) can fail to be

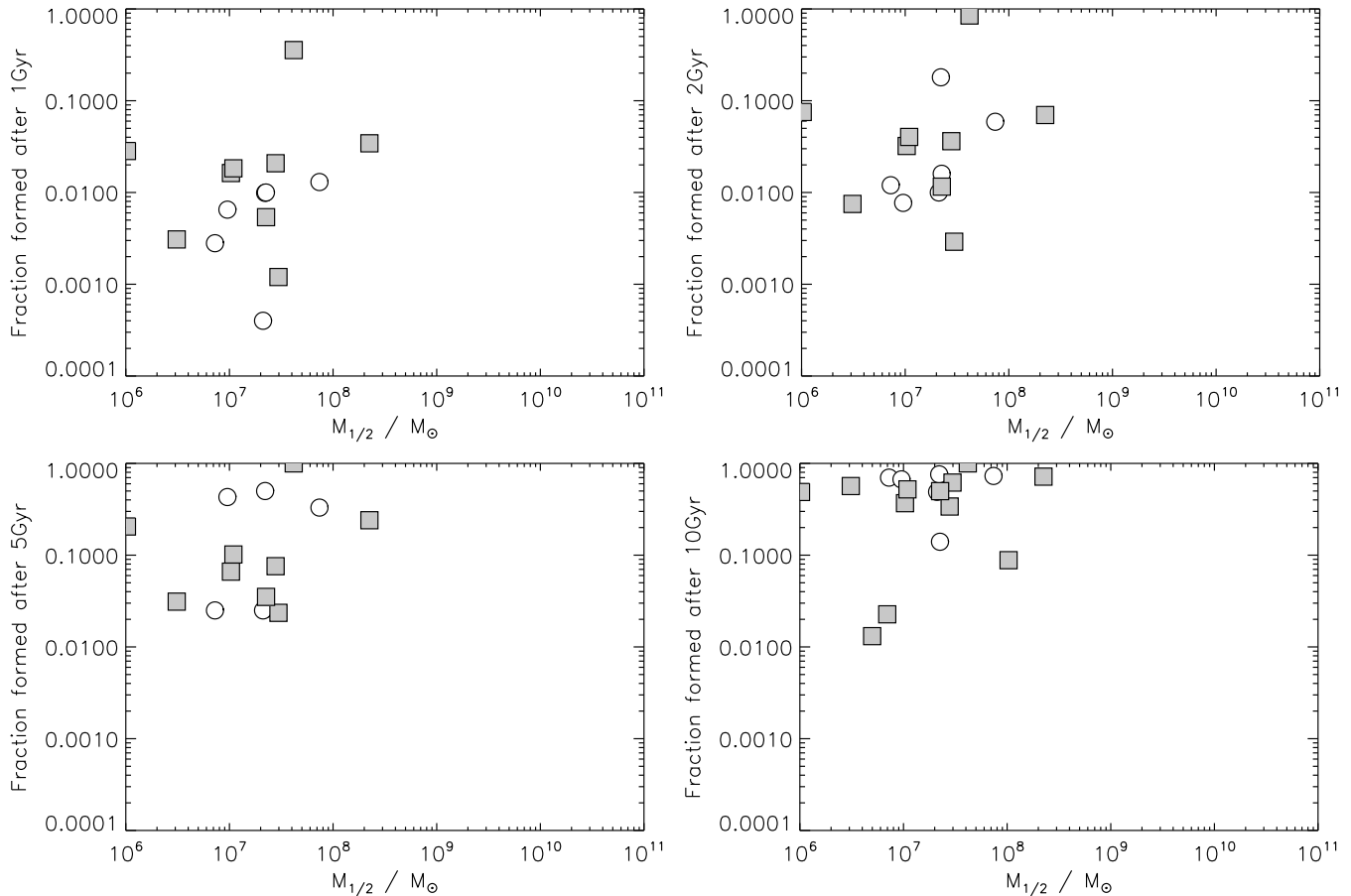


Figure 20. Star formation histories of satellite galaxies in the Reference run (grey squares) compared to values deduced from observations of Milky Way satellites (Orban et al. (2008) and Wolf et al. (2010): white circles). Each panel shows the fraction of stellar mass formed between $z = 0$ and the lookback time indicated on ordinate axis against the half stellar mass of the galaxy at $z = 0$. Stellar fractions and masses in each plot match well with the values estimated from observations, suggesting that the star formation histories of satellite galaxies in the Reference run do not wildly differ from those of observed Milky Way satellites.

detected. In any case, including a DM sub-halo host with a mass just below our mass resolution threshold ($2.2 \times 10^6 M_{\odot}$) does not affect the results we present here.

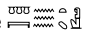
Figure 19 shows a plot comparing the half stellar mass against half-light radius of our simulated satellite galaxies (grey squares), to the satellite galaxies of the Milky Way (from Wolf et al. (2010)) (white circles) and M31 (from Collins et al. (2011, 2010); Ferguson et al. (2000); Irwin et al. (2008); Irwin & Collins (2011, priv. comm.); Kalirai et al. (2010); Letarte et al. (2009); Martin et al. (2009); McConnachie et al. (2008); Morrison et al. (2003); Pustilnik et al. (2008); Richardson et al. (2011)) (white squares). The population of simulated galaxies lie in the same region as the observed satellites except for the two galaxies labelled *a* and *h* on the figure, which lie well above the observational data. These are the most massive galaxies in our sample, which have recently been captured by the Milky Way host halo and thus have not experienced significant stripping by $z = 0$. We note that beyond their larger stellar half mass, which can be somewhat overlooked since the data from Wolf et al. (2010) do not contain the LMC or SMC, these simulated galaxies seem too compact when compared to the rather well defined observational relation linking satellites size and mass. While resolution undoubt-

edly plays an important role in getting accurate estimates of the sizes of simulated objects, it is nevertheless striking that satellite galaxies which lie on top of the observed results have all experienced tidal stripping to an advanced degree (see e.g. Figs 13 and 14). In other words, in our Reference run (which, once again, does not include feedback) every satellite galaxy which has experienced a large amount of tidal stripping falls remarkably close to the observed stellar mass - size relation.

Moreover, when we compare star formation histories of satellite galaxies in the Reference run with those derived from the analysis of colour-magnitude diagrams (CMDs) of Milky Way satellite galaxies observed by Orban et al. (2008) we find reasonable agreement. This is demonstrated in Fig. 20, where we plot the fraction of stars formed after lookback times of 1Gyr, 2Gyr, 5Gyr and 10Gyr both in simulated (grey squares) and observed (white circles) galaxies. It is somewhat reassuring that the star formation histories of our simulated satellite galaxies are broadly correct since we have previously shown (Fig 4) that they are fairly independent of resolution. Perhaps more importantly, this agreement also suggests that feedback, whatever its form and origin, cannot drastically alter the star formation histories of these galaxies: models where significant feedback at

$z > 1$ completely quenches late star formation are clearly ruled out by the observational data. This makes it all the more challenging for stellar feedback to soften cusps of dark matter sub-halos and certainly favours a rapid, irreversible mechanism, very localised in time such as the one suggested by Pontzen & Governato (2012).

5 DISCUSSION AND CONCLUSIONS

The work discussed in this paper has made use of the  suite of high (a few tens of parsec) to ultra-high (sub-parsec) resolution cosmological hydrodynamic re-simulations to investigate the effect of baryonic physics on the evolution of a ‘Milky Way’ and its satellite galaxies. Whilst various other authors have simulated satellites of Milky Way-like galaxies down to $z = 0$, ours are the first to reach sub-parsec resolution down to the end of the epoch of reionisation. The motivation for this was to analyse in detail the evolution of satellite galaxies around the epoch of reionisation, which has been posited as a mechanism for suppressing star and galaxy formation in dwarf halos and hence for shaping the population of satellite galaxies that we observe around the Milky Way and M31. To the best of our knowledge, we are also the first authors to use an adaptive mesh refinement (AMR) technique to study the evolution of these satellite galaxies down to $z = 0$ (other studies thus far either used smoothed particle hydrodynamics (SPH), or ended their simulations at higher redshifts).

In agreement with e.g. Guo et al. (2010); Ricotti & Gnedin (2005); Wadepuhl & Springel (2010), we find that reionisation appears not to efficiently stop star, or even galaxy formation. Instead, we find that satellite galaxy formation continues down to at least $z = 4.8$ in our lowest (~ 50 pc) resolution simulation. The number of luminous satellite galaxies formed before reionisation ($z = 8.5$ in our case) is found to be far lower than the number of observed Milky Way satellites. These results are consistent with e.g. Okamoto & Frenk (2009); Hoefl et al. (2006): like these authors, we find that, down to the end of the reionisation era, there exists a threshold in v_{max} of about 10 km/s below which halos remain dark, never forming stars. This threshold persists at later redshifts, i.e. well after reionisation has ended. This is probably due to the fact that efficient atomic gas cooling increases halo central densities and hence v_{max} , separating halos that can cool gas and form stars from those that cannot. There are, however, at least two major limitations in our work that prevent us from commenting further. First, we do not run a simulation with self-consistent star formation and ionisation, and hence we cannot quantify the precise effect of UV photoionisation on star formation in galaxies already forming stars. Secondly, our model of reionisation consists of a uniform background which neglects the effect of gas self-shielding from external photoionisation sources. Future studies which include ionising photon radiative transfer and hence self-consistent re-ionisation, should allow us to determine whether proximity effects and/or self-shielding significantly alter our conclusions, but this does not seem likely.

The effect of supernova feedback on the gas and stellar mass of high redshift (both pre- and post-reionisation)

galaxies seems to be quite stochastic. Indeed, our results exhibit a large scatter, even though one might argue we detect a slight systematic trend of star formation being enhanced by feedback as galaxy mass increases. A key feature of our model of supernova feedback is that it consists of star particles (with a standard Salpeter IMF) injecting mass, energy, momentum and metals into the surrounding gas according to a Sedov blast wave solution deposited onto the grid 10Myr after they have formed. Together with our sub-parsec resolution, this means that we should be able to track the effect of supernovae explosions fairly realistically on scales typical of small molecular clouds. Outflows and heating from these supernovae reduce the amount of gas available for star formation, but blast wave compression and an excess of radiative cooling due to the injection of metals into the ISM can potentially increase it. Our results show that, on average, adding supernovae feedback does reduce the gas and stellar mass of galaxies in halos below $10^9 M_\odot$ (negative feedback) but increases it for galaxies hosted by halos above $10^9 M_\odot$, where the deeper potential and extra metal injection negates the impact of outflows (positive feedback). In any case, the stellar masses of individual galaxies are only changed by maximum 10-20 percent either way by supernova feedback, and one has to invoke a much larger energetic input (for example a top-heavy IMF, or a large fraction of hypernovae) and/or one that is impervious to radiative losses (e.g. some kind of ‘turbulent’ energy) to overturn the situation in favour of negative feedback.

When we use lower resolution (50 pc) runs to track the descendants of galaxies in the high resolution (0.5 pc) Cooling and Feedback runs to $z = 0$, we find that very few of the galaxies which are captured by the Milky Way progenitor halo survive to $z = 0$. In fact, independent of the run used to perform the tracking (PureDM, Adiabatic or Reference), no satellite galaxy captured by the Milky Way progenitor before $z = 3$ survives as Milky Way satellite at $z = 0$. However, the main difference is that *all* galaxies (sub-halos) captured *after* $z = 3$ in the Pure DM or Adiabatic runs survive, while only a small fraction of these does so in the Reference run. This is caused by the much higher central density of the Milky Way halo (and sub-halos) in the Reference run (the only one to host a MW galaxy), which significantly shortens the dynamical friction timescales for satellites to spiral to the centre of the halo and experience disruption. We note that this result is still a matter of debate in the recent literature, with Libeskind et al. (2010) and Romano-Díaz et al. (2010, 2009); Schewtschenko & Macciò (2011), all using a very similar tree-SPH technique, reaching different conclusions. Whereas the former group of authors seem to disagree with us, the latter report a higher destruction rate of satellites when baryons and cooling are included in their simulations, consistent with our finding. We believe that the work presented here, which makes use of a completely different simulation technique and improves on the resolution of these previous studies, sheds a useful light on the issue. In particular, we emphasize that when we compare properties of the remaining satellite galaxies at $z = 0$ in the Reference run to their observational equivalents for the Milky Way or M31, we find that the star formation histories, stellar masses and half-light radii are in reasonable agreement. Only the more massive, recently captured satellites are found to be too compact when compared to Milky Way and M31 dwarf

spheroidal satellites. This puts rather tight constraints on the feedback mechanisms (amount of energy, duration, timing) required to soften the cusps of dark matter halos as they cannot have a major impact on these properties.

Finally, beyond the importance of the role played by baryonic physics in determining the number of satellites of MW class halos, our study also highlights the extreme sensitivity of this number to the circular velocity of the host halo. Whilst all simulated CDM halos in the literature match the shape of the $N_{\text{sat}} \propto V_{\text{max}}^3$ relation from Reed et al. (2005), not all of them agree on the constant of normalisation. Indeed, our Pure DM run agrees with the normalisation given by Reed et al. (2005) at the 10-20 % level whereas the Aquarius (Springel et al. 2008) simulations overshoot it by a factor ~ 3 , and by about 30 % more than the Via Lactea II (Diemand et al. 2008) simulation. Curiously enough, the cause of this significant discrepancy is still unresolved, even though the debate has received a lot of attention lately in papers such as Vera-Ciro et al. (2011); Boylan-Kolchin et al. (2012); Wang et al. (2012). Irrespective of this disagreement, our results, especially when baryonic physics is taken into account, argue in favour of a rather light ($5 \times 10^{11} M_{\odot} < M_{\text{vir}} < 10^{12} M_{\odot}$) MW halo. Note that if the likelihood for a satellite galaxy to survive down to $z = 0$ is suppressed by even half as much as we find in this work when feedback is properly incorporated, models relying on N-body dark matter-only simulations, such as semi-analytic models (SAMs) should be revised accordingly.

6 ACKNOWLEDGEMENTS

The authors would like to thank Romain Teyssier and Taysun Kimm for useful comments and discussions during the production of this paper. The simulations presented here have run partly on the JADE supercomputer at the *Centre Informatique National de l'Enseignement Supérieure* (on resources allocated to project number GEN2191), and partly on the DiRAC facility jointly funded by STFC, the Large Facilities Capital Fund of BIS and the University of Oxford. We warmly thank Jonathan Patterson for his phenomenal help in using the latter. The authors would also like to thank Michelle Collins and Mike Irwin for allowing them to use their collated M31 satellite data, and Dylan Tweed for making his merger tree code available. We also acknowledge the Royal Astronomical Society for funding in support of this research. SG is funded by a STFC studentship and a Cosmocomp fellowship. JD and AS's research is supported by Adrian Beecroft, the Oxford Martin School and the STFC.

REFERENCES

Agertz O., Moore B., Stadel J., Potter D., Miniati F., Read J., Mayer L., Gawryszczak A., Kravtsov A., Nordlund A. k., Pearce F., Quilis V., Rudd D., Springel V., Stone J., Tasker E., Teyssier R., Wadsley J., Walder R., 2007, *Monthly Notices of the Royal Astronomical Society*, 380, 963
 Assousa G. E., Herbst W., 1980, In: *Giant molecular clouds in the Galaxy; Proceedings of the Third Gregynog Astrophysics Workshop*, pp 275–284

Battaglia G., Helmi A., Morrison H., Harding P., Olszewski E. W., Mateo M., Freeman K. C., Norris J., Shectman S. A., 2005, *Monthly Notices of the Royal Astronomical Society*, 364, 433
 Bekki K., Chiba M., 2005, *Monthly Notices of the Royal Astronomical Society*, 356, 680
 Bekki K., Stanimirović S., 2009, *Monthly Notices of the Royal Astronomical Society*, 395, 342
 Belokurov V., Walker M. G., Evans N. W., Gilmore G., Irwin M. J., Just D., Koposov S., Mateo M., Olszewski E., Watkins L., Wyrzykowski L., 2010, *The Astrophysical Journal Letters*, 712, L103
 Benson A. J., Bower R. G., Frenk C. S., Lacey C. G., Baugh C. M., Cole S., 2003, *The Astrophysical Journal*, 599, 38
 Benson A. J., Lacey C., Baugh C., Cole S., Frenk C., 2002, *Extragalactic Gas at Low Redshift*, 254, 354
 Bertschinger E., 2001, *The Astrophysical Journal Supplement Series*, 137, 1
 Binney J., Tremaine S., 2008, *Galactic Dynamics: Second Edition*
 Blumenthal G. R., Faber S. M., Primack J. R., Rees M. J., 1984, *Nature*, 311, 517
 Boylan-Kolchin M., Bullock J. S., Kaplinghat M., 2011, *Monthly Notices of the Royal Astronomical Society: Letters*, 415, L40
 Boylan-Kolchin M., Bullock J. S., Kaplinghat M., 2012, *Monthly Notices of the Royal Astronomical Society*, -1, no
 Bullock J. S., Kravtsov A. V., Weinberg D. H., 2000, *The Astrophysical Journal*, 539, 517
 Busha M. T., Alvarez M. A., Wechsler R. H., Abel T., Strigari L. E., 2010, *The Astrophysical Journal*, 710, 408
 Cen R., McDonald P., Trac H., Loeb A., 2009, *The Astrophysical Journal Letters*, 706, L164
 Cen R., Ostriker J. P., 1992, *Astrophysical Journal*, 399, L113
 Ceverino D., Klypin A., 2009, *The Astrophysical Journal*, 695, 292
 Collins M. L. M., Chapman S. C., Irwin M. J., Martin N. F., Ibata R. A., Zucker D. B., Blain A., Ferguson A. M. N., Lewis G. F., McConnachie A. W., Peñarrubia J., 2010, *Monthly Notices of the Royal Astronomical Society*, 407, 2411
 Collins M. L. M., Chapman S. C., Rich R. M., Irwin M. J., Peñarrubia J., Ibata R. A., Arimoto N., Brooks A. M., Ferguson A. M. N., Lewis G. F., McConnachie A. W., Venn K., 2011, *Monthly Notices of the Royal Astronomical Society*, 417, 1170
 Dekel A., Silk J., 1986, *Astrophysical Journal*, 303, 39
 Dekel A., Woo J., 2003, *Monthly Notices of the Royal Astronomical Society*, 344, 1131
 Di Cintio A., Knebe A., Libeskind N. I., Yepes G., Gottlöber S., Hoffman Y., 2011, *Monthly Notices of the Royal Astronomical Society: Letters*, -1, no
 Diemand J., Kuhlen M., Madau P., Zemp M., Moore B., Potter D., Stadel J., 2008, *Nature*, 454, 735
 Dubois Y., Teyssier R., 2008, *Astronomy and Astrophysics*, 477, 79
 Dunkley J., Komatsu E., Nolte M. R., Spergel D. N., Larson D., Hinshaw G., Page L., Bennett C. L., Gold B., Jarosik N., Weiland J. L., Halpern M., Hill R. S., Kogut A., Limon M., Meyer S. S., Tucker G. S., Wollack E.,

- Wright E. L., 2009, *The Astrophysical Journal Supplement*, 180, 306
- Efstathiou, G. 1992, *Monthly Notices of the Royal Astronomical Society* (ISSN 0035-8711), 256
- Ferguson A. M. N., Gallagher J. S., Wyse R. F. G., 2000, *The Astronomical Journal*, 120, 821
- Flores R. A., Primack J. R., 1994, *The Astrophysical Journal*, 427, L1
- Gnedin N. Y., 2000, *The Astrophysical Journal*, 542, 535
- Gnedin N. Y., Kravtsov A. V., 2006, *The Astrophysical Journal*, 645, 1054
- Guo Q., White S., Li C., Boylan-Kolchin M., 2010, *Monthly Notices of the Royal Astronomical Society*, 404, 1111
- Haardt F., Madau P., 1996, *Astrophysical Journal* v.461, 461, 20
- Hoeft M., Yepes G., Gottlöber S., Springel V., 2006, *Monthly Notices of the Royal Astronomical Society*, 371, 401
- Irwin M. J., Collins M. L. M., 2011, private communication
- Irwin M. J., Ferguson A. M. N., Huxor A. P., Tanvir N. R., Ibata R. A., Lewis G. F., 2008, *The Astrophysical Journal*, 676, L17
- Kalirai J. S., Beaton R. L., Geha M. C., Gilbert K. M., Guhathakurta P., Kirby E. N., Majewski S. R., Ostheimer J. C., Patterson R. J., Wolf J., 2010, *The Astrophysical Journal*, 711, 671
- Karachentsev I. D., Kashibadze O. G., 2005, *Astrofizica*
- Kimm T., Devriendt J., Slyz A., Pichon C., Kassim S. A., Dubois Y., 2011, eprint arXiv, 1106, 538
- Kirby E. N., Martin C. L., Finlator K., 2011, *The Astrophysical Journal*, 742, L25
- Kitayama T., Susa H., Umemura M., Ikeuchi S., 2001, *Monthly Notices of the Royal Astronomical Society*, 326, 1353
- Knebe A., Knollmann S. R., Muldrew S. I., Pearce F. R., Aragon-Calvo M. A., Ascasibar Y., Behroozi P. S., Ceverino D., Colombi S., Diemand J., Dolag K., Falck B. L., Fasel P., Gardner J., Gottlöber S., 2011, *Monthly Notices of the Royal Astronomical Society*
- Koposov S., Belokurov V., Evans N. W., Hewett P. C., Irwin M. J., Gilmore G., Zucker D. B., Rix H.-W., Fellhauer M., Bell E. F., Glushkova E. V., 2008, *The Astrophysical Journal*, 686, 279
- Kravtsov A. V., Gnedin O. Y., Klypin A. A., 2004, *The Astrophysical Journal*, 609, 482
- Larson D., Dunkley J., Hinshaw G., Komatsu E., Nolte M. R., Bennett C. L., Gold B., Halpern M., Hill R. S., Jarosik N., Kogut A., Limon M., Meyer S. S., Odegard N., Page L., Smith K. M., Spergel D. N., Tucker G. S., Weiland J. L., Wollack E., Wright E. L., 2010, eprint arXiv, 1001, 4635
- Letarte B., Chapman S. C., Collins M., Ibata R. A., Irwin M. J., Ferguson A. M. N., Lewis G. F., Martin N., McConnachie A., Tanvir N., 2009, *Monthly Notices of the Royal Astronomical Society*, 400, 1472
- Libeskind N. I., Yepes G., Knebe A., Gottlöber S., Hoffman Y., Knollmann S. R., 2010, *Monthly Notices of the Royal Astronomical Society*, 401, 1889
- Lovell M. R., Eke V., Frenk C. S., Gao L., Jenkins A., Theuns T., Wang J., White S. D. M., Boyarsky A., Ruchayskiy O., 2012, *Monthly Notices of the Royal Astronomical Society*, 420, 2318
- Low M.-M. M., Ferrara A., 1999, *The Astrophysical Journal*, 513, 142
- Macciò A. V., Kang X., Fontanot F., Somerville R. S., Koposov S., Monaco P., 2010, *Monthly Notices of the Royal Astronomical Society*, 402, 1995
- McConnachie A. W., Huxor A., Martin N. F., Irwin M. J., Chapman S. C., Fahlman G., Ferguson A. M. N., Ibata R. A., Lewis G. F., Richer H., Tanvir N. R., 2008, *The Astrophysical Journal*, 688, 1009
- Machacek M. E., Bryan G. L., Abel T., 2001, *The Astrophysical Journal*, 548, 509
- Madau P., Diemand J., Kuhlen M., 2008, *The Astrophysical Journal*, 679, 1260
- Madau P., Kuhlen M., Diemand J., Moore B., Zemp M., Potter D., Stadel J., 2008, *The Astrophysical Journal*, 689, L41
- Martin N. F., McConnachie A. W., Irwin M., Widrow L. M., Ferguson A. M. N., Ibata R. A., Dubinski J., Babul A., Chapman S., Fardal M., Lewis G. F., Navarro J., Rich R. M., 2009, *The Astrophysical Journal*, 705, 758
- Mashchenko S., Wadsley J., Couchman H. M. P., 2008, *Science*, 319, 174
- Mateo M. L., 1998, *Annual Review of Astronomy and Astrophysics*, 36, 435
- Mesinger A., Furlanetto S., 2009, *Monthly Notices of the Royal Astronomical Society*, 400, 1461
- Mitchell N. L., McCarthy I. G., Bower R. G., Theuns T., Crain R. A., 2009, *Monthly Notices of the Royal Astronomical Society*, 395, 180
- Moore B., Diemand J., Madau P., Zemp M., Stadel J., 2006, *Monthly Notices of the Royal Astronomical Society*, 368, 563
- Moore B., Ghigna S., Governato F., Lake G., Quinn T., Stadel J., Tozzi P., 1999, *The Astrophysical Journal*, 524, L19
- Morrison H. L., Harding P., Hurley-Keller D., Jacoby G., 2003, *The Astrophysical Journal*, 596, L183
- Muñoz J. A., Madau P., Loeb A., Diemand J., 2009, *Monthly Notices of the Royal Astronomical Society*, 400, 1593
- Murante G., Monaco P., Giovali M., Borgani S., Diaferio A., 2010, *Monthly Notices of the Royal Astronomical Society*, 405, 1491
- Nickerson S., Stinson G., Couchman H. M. P., Bailin J., Wadsley J., 2011, *Monthly Notices of the Royal Astronomical Society*, p. 662
- Okamoto T., Frenk C. S., 2009, *Monthly Notices of the Royal Astronomical Society: Letters*, 399, L174
- Okamoto T., Gao L., Theuns T., 2008, *Monthly Notices of the Royal Astronomical Society*, 390, 920
- Orban C., Gnedin O. Y., Weisz D. R., Skillman E. D., Dolphin A. E., Holtzman J. A., 2008, *The Astrophysical Journal*, 686, 1030
- Parry O. H., Eke V. R., Frenk C. S., Okamoto T., 2012, *Monthly Notices of the Royal Astronomical Society*, 419, 3304
- Peñarrubia J., Benson A. J., Walker M. G., Gilmore G., McConnachie A. W., Mayer L., 2010, *Monthly Notices of the Royal Astronomical Society*, 406, 1290
- Peirani S., 2010, *Monthly Notices of the Royal Astronomical Society*, 407, 1487
- Pontzen A., Governato F., 2012, *Monthly Notices of the*

- Royal Astronomical Society, 421, 3464
- Powell L. C., Slyz A., Devriendt J., 2011, *Monthly Notices of the Royal Astronomical Society*, 414, 3671
- Prunet S., Pichon C., Aubert D., Pogosyan D., Teyssier R., Gottloeber S., 2008, *The Astrophysical Journal Supplement Series*, 178, 179
- Pustilnik S. A., Tepliakova A. L., Kniazev A. Y., Burenkov A. N., 2008, *Astrophysical Bulletin*, 63, 102
- Quinn T., Katz N., Efstathiou G., 1996, *Monthly Notices of the Royal Astronomical Society*, 278
- Rasera Y., Teyssier R., 2006, *Astronomy and Astrophysics*, 445, 1
- Reed D., Governato F., Quinn T., Gardner J., Stadel J., Lake G., 2005, *Monthly Notices of the Royal Astronomical Society*, 359, 1537
- Richardson J. C., Irwin M. J., McConnachie A. W., Martin N. F., Dotter A. L., Ferguson A. M. N., Ibata R. A., Chapman S. C., Lewis G. F., Tanvir N. R., Rich R. M., 2011, *The Astrophysical Journal*, 732, 76
- Ricotti M., Gnedin N. Y., 2005, *The Astrophysical Journal*, 629, 259
- Ricotti M., Gnedin N. Y., Shull J. M., 2008, *The Astrophysical Journal*, 685, 21
- Romano-Díaz E., Shlosman I., Heller C., Hoffman Y., 2009, *The Astrophysical Journal*, 702, 1250
- Romano-Díaz E., Shlosman I., Heller C., Hoffman Y., 2010, *The Astrophysical Journal*, 716, 1095
- Salpeter E. E., 1955, *Astrophysical Journal*, 121, 161
- Sawala T., Scannapieco C., White S., 2012, *Monthly Notices of the Royal Astronomical Society*, 420, 1714
- Scannapieco C., Tissera P. B., White S. D. M., Springel V., 2005, *Monthly Notices of the Royal Astronomical Society*, 364, 552
- Scannapieco C., Tissera P. B., White S. D. M., Springel V., 2006, *Monthly Notices of the Royal Astronomical Society*, 371, 1125
- Scannapieco C., White S. D. M., Springel V., Tissera P. B., 2011, *Monthly Notices of the Royal Astronomical Society*, 417, 154
- Schewtschenko J. A., Macciò A. V., 2011, *Monthly Notices of the Royal Astronomical Society*, 413, 878
- Simon J. D., Geha M., 2007, *The Astrophysical Journal*, 670, 313
- Slyz A. D., Devriendt J. E. G., Bryan G., Silk J., 2005, *Monthly Notices of the Royal Astronomical Society*, 356, 737
- Somerville R. S., 2002, *The Astrophysical Journal*, 572, L23
- Springel V., 2005, *Monthly Notices of the Royal Astronomical Society*, 364, 1105
- Springel V., Wang J., Vogelsberger M., Ludlow A., Jenkins A., Helmi A., Navarro J. F., Frenk C. S., White S. D. M., 2008, *Monthly Notices of the Royal Astronomical Society*, 391, 1685
- Stinson G. S., Dalcanton J. J., Quinn T., Kaufmann T., Wadsley J., 2007, *The Astrophysical Journal*, 667, 170
- Strigari L. E., Bullock J. S., Kaplinghat M., Diemand J., Kuhlen M., Madau P., 2007, *The Astrophysical Journal*, 669, 676
- Strigari L. E., Bullock J. S., Kaplinghat M., Simon J. D., Geha M., Willman B., Walker M. G., 2008, *Nature*, 454, 1096
- Susa H., Umemura M., 2004, *The Astrophysical Journal*, 610, L5
- Tassis K., Kravtsov A. V., Gnedin N. Y., 2008, *The Astrophysical Journal*, 672, 888
- Teyssier R., 2002, *Astronomy and Astrophysics*, 385, 337
- Tollerud E. J., Bullock J. S., Strigari L. E., Willman B., 2008, *The Astrophysical Journal*, 688, 277
- Tolstoy E., Hill V., Tosi M., 2009, *Annual Review of Astronomy and Astrophysics*, 47, 371
- Tweed D., Devriendt J., Blaizot J., Colombi S., Slyz A., 2009, *Astronomy and Astrophysics*, 506, 647
- Vera-Ciro C. A., Sales L. V., Helmi A., Frenk C. S., Navarro J. F., Springel V., Vogelsberger M., White S. D. M., 2011, *Monthly Notices of the Royal Astronomical Society*, 416, 1377
- Wadepuhl M., Springel V., 2010, *Monthly Notices of the Royal Astronomical Society*, 410, no
- Wang J., Frenk C. S., Navarro J. F., Gao L., 2012, eprint arXiv:1203.4097
- Watkins L. L., Evans N. W., An J. H., 2010, *Monthly Notices of the Royal Astronomical Society*, 406, 264
- Wilkins S. M., Bunker A. J., Lorenzoni S., Caruana J., 2011, *Monthly Notices of the Royal Astronomical Society*, 411, 23
- Wolf J., Martinez G. D., Bullock J. S., Kaplinghat M., Geha M., Muñoz R. R., Simon J. D., Avedo F. F., 2010, *Monthly Notices of the Royal Astronomical Society*, p. 778